Functional connectivity, structural connectivity, and inter-individual variability in *Drosophila melanogaster*

Takuto Okuno[a,b*], Alexander Woodward[c], Hideyuki Okano[b,d], Junichi Hata[a,b]

[a] *Graduate School of Human Health Sciences, Tokyo Metropolitan University, 7-2-10 Higashiogu, Arakawa-ku, Tokyo, 116-8551, Japan*

[b] *Laboratory for Marmoset Models of Brain Diseases, RIKEN Center for Brain Science, 2-1 Hirosawa, Wako, Saitama 351-0198, Japan*

[c] *Intelligent Vision Systems Lab, The University of Auckland, 34 Princes Street, Auckland Central, Auckland 1010, New Zealand*

[d] *Keio University Regenerative Medicine Research Center, Kawasaki 210-0821, Kanagawa, Japan.*

* *Corresponding author*

Abstract

Clarifying the relationship between structure and function is important for understanding the brain. In *Drosophila melanogaster*, whole-brain and hemibrain electron microscopy connectome data, as well as whole-brain calcium imaging data are available. We applied pre-processing methods from fMRI to whole-brain calcium imaging data and comprehensively investigated the optimal parameters. Then, we found that the FC-SC (functional and structural connectivity) correlation decreased linearly with ROI count, and this trend was the same in flies and humans. We also developed a new, more robust method to quantify the degree of pre- and post-synaptic segregation and investigated this in the fly whole-brain. This revealed that many neurons have unsegregated synapses. We extracted highly unsegregated synapses and compared them with random-extracted null SC matrices. Their FC-SC correlation was significantly higher, indicating that these synapses contribute to FC well. Conversely, highly segregated-synapses showed significantly lower FC-SC correlation and contribute less to FC. Therefore, neurons with unsegregated synapses like non-spiking neurons are spread throughout the whole brain, and they are thought to have a significant influence on FC.

Introduction (Main text – up to 5,000 words)

Functional connectivity (FC) describes the relationship between functional activity in one brain region and that in another. In previous approaches, two spike trains were analyzed by a cross-correlation histogram [1, 2]; then, this method was applied to positron emission tomography and functional magnetic resonance imaging (fMRI) [3]. Subsequently, the time-series correlation between two regions has become widely used as a measure of undirected FC [4]. Underlying such functional connectivity, a structural connectivity (SC) substrate exists, and its relationship with FC has been investigated using various modalities [5, 6, 7, 8, 9, 10, 11]. In humans, FC-SC correlations between resting-state (rs-) fMRI and diffusion tensor imaging have been explored, and studies have shown high relationships of r=0.66 for 66 regions and r=0.54 for 998 regions [6, 7]. Other studies have examined the relationship between rs-fMRI and SC based on retrograde tracing from 145 injection sites in the left cortex of marmosets (r=0.379 for 9862 voxels, Ext.Data.Fig.2-1c) [10] and the relationship between calcium imaging and SC based on electron microscopy (EM) in the hemibrain of *Drosophila melanogaster (D. melanogaster)* [12] (r=0.74 for 37 regions) [9]. Because of the disparity in species, number of ROIs, and modalities, a direct comparison across them becomes difficult. Therefore, in this study, we used whole-brain [13] and hemibrain [12] EM connectome data, which are currently considered to be the most detailed, and whole-brain calcium imaging data [14] of *D. melanogaster* to comprehensively investigate the relationship between FC and SC across various ROI shapes and numbers. Our results of the FC-SC correlations in the fly hemibrain compared to the human cortex at various ROIs showed roughly 1.08–1.24 times higher FC-SC correlations in the fly (Fig. 2d), and no large divergence was observed between the two species.

Because of the strong relationship between FC and SC, they can be used to investigate inter-individual variability in *D. melanogaster*. In particular, the FlyWire whole-brain and FlyEM hemibrain connectome data have been compared [15, 16], and widely different results are observed with cell typing [16]. However, these studies have yet to clarify whether these differences in connectome between the two individuals are attributed to inter-individual variability or some other reasons. Therefore, we compared these two EM connectomes based on the averaged FC of eight flies. FlyEM was scanned at a resolution of

8×8×8 nm, and the connectome data has a “confidence” threshold that indicates the degree of synaptic detection. Conversely, FlyWire was scanned at a resolution of 4×4×40 nm, and it had a “CleftScore” [17] threshold that shows the degree of synaptic detection. In fact, the thresholds initially employed by FlyWire and FlyEM caused large differences in post-synapse numbers; as such, we adjusted for the thresholds and compared the EM connectome data in each fly. We found that FlyEM clearly had higher values (more accuracy) than FlyWire in its FC-SC correlation and detection. In our judgment, this difference was not caused by inter-individual variability; instead, it was attributed to differences in the accuracy of detection and annotation of dendrites, axons, and synapses because of the voxel anisotropy.

We explored how functional activity contributed to the FC. In textbook terms, post-synapses on dendrites receive neurotransmitters and conduct an action potential along nerve fibers if they are excitatory; and pre-synapses on axons release neurotransmitters [18, 19]. In calcium imaging, the pre-synaptic activity in each region is detected as calcium signals, which represent functional activity. Then the FC is detected as the synchronization of functional activities. However, the synaptic arrangement on the neurons revealed in the EM connectome shows pre- and post-synapses that are highly intermingled in many neurons (i.e. input and output locations may be intermingled across axon and dendritic arbors); thus, signal transmission may be complex [19, 15, 13, 20]. Nerve cells include non-spiking neurons such as visual neurons, CT1 amacrine cells [21, 22, 23, 24, 25], interneurons in the antennal lobe [26], and APL cells in the mushroom body [27, 28, 29]. In *D. melanogaster*. these cells show localized functional activity taking place on a portion of the dendrite. In CT1 and APL cells, the pre- and post-synapses are highly intermingled (Fig.4a, Ext.Data.Fig.4-2). Therefore, we wanted to investigate the presence of these unsegregated synapse-type neurons in the brain. We defined the pre- and post-synapse segregation index (PPSSI) and found that only some cells have a clear synaptic segregation, and many neurons have unsegregated synapses. When we extracted synapses with a particularly low segregation (high intermingling) and compared them between SC and FC, we found a significantly higher FC-SC correlation. Conversely, neurons with a high segregation had significantly lower FC-SC correlations.

Many *Drosophila* brain neurons are interconnected [30]. As such, we similarly investigated reciprocal synapses [31, 32, 33, 34, 35], whose function is clearer than that of other unsegregated synapse types. When we extracted such reciprocal synapses, the FC-SC correlation was significantly higher. Our results indicated that unsegregated synapses contributed more to the FC. In other words, local activity due to unsegregated synapses could be considered the more essential functional activity. Unsegregated synapses are found not only in flies but also in mammals [31, 32, 18, 36, 37, 38], including humans (Ext.Data.Fig.1-2 from [39]). Localized functional activity from pre-synaptic population dynamics can be observed by calcium imaging or detected through the neurovascular coupling with astrocytes [40] via fMRI. Although modalities vary, the FC-SC correlation between humans and flies does not considerably differ, as shown earlier. Since various fMRI pre-processing and analysis methods can be directly applied to pre-synaptic population dynamics in this study, functional activity is locally compartmentalized in the whole brain, which is common among various species.

Results

Investigation of the optimal nuisance factor removal method for calcium imaging

First, the optimal pre-processing of the calcium imaging data of *D. melanogaster* was investigated. The registration method used in fMRI was applied to the calcium image (Ext.Data.Fig.1-1) to register to the FDA template [14] (Fig. 1b). Then, various nuisance factor removal methods (details in Methods) were applied to the ROI time-series to generate the FC matrices of eight flies (Fig. 1a). Three types of ROIs were used in the analysis: ROIs based on the anatomical neuropil, commonly used in *Drosophila* (hemibrain ROI), ROIs based on k-means clustering of the SC matrix of 146,604 voxels in the hemibrain (SCKm), and ROIs based on distance-based clustering of voxels in the hemibrain (DistKm). SCKm can provide ROIs close to the shape of the anatomical neuropil across various ROI counts (Ext.Data.Fig.2-1a), while DistKm can provide ROIs that are completely unrelated to the anatomical neuropil. Next, a correlation analysis and ROC curve analysis were performed using the SC matrices based on FlyEM and the FC matrices with these ROI types (Fig. 1a). Fig. 1d-f shows the FC-SC correlation results, FC-SC

detection results, and the normalized total score of FC-SC detection and correlation (details in Methods), respectively. After the comparison of the raw (leftmost) and removal methods for various ROI types, the combination of polynomial detrending [41] & tCompCor [42] was found to yield the optimal results. The optimal removal methods were found to differ between fMRI [10] and calcium imaging data, and these results are further described in the Discussion section.

Comparison of the FC-SC correlation between humans and flies

Spatial smoothing is useful for absorbing inter-individual variability and conducting second-level group analysis [10, 43]. Here, we explored the effect of spatial smoothing (of the calcium imaging data) on various ROI counts in DistKm (Fig. 2a) and SCKm (Ext.Data.Fig.2-1a) ROIs. In DistKm, smoothing was highly effective, and the optimal kernel radius of the Gaussian filter was around 23 voxels (52.44 μm) for various ROI counts (Fig. 2b). In SCKm, smoothing was ineffective for ROI count below 100, while the kernel radius above 16 voxels (36.48 μm) was effective for ROI count above 100 (Ext.Data.Fig.2-1b). SCKm has a larger variation in volume for each ROI count than DistKm (Fig. 1c, Fig. 2e); as such, the effect of spatial smoothing is likely unstable. Next, we investigated whether the combination of spatial smoothing and Poly-tCompCor was effective. We found that this combination was significantly more effective than smoothing alone for SCKm and DistKm (Fig. 2c, Mann–Whitney U test $p<1.67e-4$ Bonferroni corrected). Conversely, the combination of a high-pass filter and nuisance factor removal overlapped for the purpose of noise removal, and the effect was degraded (Ext.Data.Fig.2-1d), as found in fMRI [10].

The optimal FC-SC correlation for various ROI counts was determined. Results showed that the correlation decreased proportionally to the logarithm of the ROI count (Fig. 2d). This was also compared between flies and mammals. At approximately 50 ROIs, the difference was nearly 1.08-fold to 1.22-fold ($r=0.66$ for humans and $r=0.71$-0.81 for flies [SCKm, DistKm]); by contrast, at approximately 1,000 ROIs, the difference was roughly 1.12-fold to 1.24-fold ($r=0.54$ for humans and $r=0.6$-0.67 for flies), which was

not a considerable difference. The difference was slightly larger (1.21 to 1.5-fold: r=0.378 for marmosets and r=0.46-0.57 for flies) than the marmoset results at around 10,000 ROIs (Ext.Data.Fig.2-1c). Although SCs for flies and humans were obtained from single individuals, the tracer data is a composite from 52 marmosets [44], which might contribute to the difference with the fly's FC-SC correlation.

Comparison between FlyEM and FlyWire connectome data

We used the FlyEM's SC to compare the averaged FC of eight flies. In this section, we also used the FlyWire connectome data [45] to compare the FC and each SC, and possibly reveal the inter-individual variability of the two EM connectome data. As mentioned earlier, FlyEM has a synaptic "confidence" threshold and contains 21.4 million post-synapses in the hemibrain region at its initial value of 0. Conversely, FlyWire has a 'CleftScore' [17] threshold and 18.8 million post-synapses at its initial value of 50. Since the number of post-synapses differs at each threshold, we set the confidence threshold of 0.8 as high as possible, thereby increasing the FC-SC correlation (Fig. 3d, ExtFig.3-1b). Then we adjusted the CleftScore to 140, which has a post-synapse number of approximately 11.4 million (Fig. 3a). These thresholds were used for all analyses in this study. When we displayed the maximum Z-projection of the synapse point cloud of post-synapse counts in each voxel, we found that the trends in synapse detection completely varied (Fig. 3b). In each region, FlyEM had more synapses in the mushroom bodies (aL, bL, etc.) and in the major neuropils of the central nervous system (CNS; EB, FB, NO, and PB). In comparison, FlyWire had more synapses in the visual system (LO and ME) and in the periesophageal neuropils (CAN and FLA; Fig. 3c). In the FC-SC correlation of each region, FlyEM had higher values in most regions at 58:5 (Fig. 3e, ExtFig.3-1a). As a result, FlyEM r=0.73 differed from FlyWire r=0.68 at the matrix level (Fig. 3d). Both datasets were from genotype Canton-S-G1×w1118 adult females; FlyEM was five-day-old [12], and FlyWire was seven-day-old [13]. Although brain development may differ depending on the rearing environment, the tendency to detect synapses substantially varied. We attribute this to differences in detection accuracy resulting from the resolution of EM scanning, but not to inter-individual variability.

We next used the FlyWire connectome data to investigate the ratios of neurotransmitter input (ExtFig.3-2a) and output (Fig. 3f) in each region. The highest percentage was acetylcholine (62.8%±14.2%), followed by glutamine (15.5%±9.2%), then GABA (11.4%±8.2%) in neurotransmitter output. The analysis of the relationship between this ratio and FC-SC correlation in each neurotransmitter revealed significant correlations for acetylcholine (r=0.39, p=0.0013) and GABA (r=-0.25, p=0.046). That is, the higher the percentage of excitatory connections, the higher the FC-SC correlation; conversely, the higher the percentage of inhibitory connections, the lower the FC-SC correlation. In humans, FC-SC correlations are lower in the evolutionarily expanded Brodmann area 39,45 and the temporal lobe [8]; therefore, these areas may have more long range inhibitory connections [46, 47, 48].

Unsegregated synapses contribute considerably to functional connectivity

We compared FC-SC in the macroscopic regions, and we also investigated the relationship between the synapses, the source of functional activity (pre-synaptic population dynamics), and FC. First, we examined the synaptic segregation in whole-brain neurons because many neurons showed pre- and post-synaptic intermingling. Then, we determined how unsegregated and segregated synapses affected the FC. To quantify synaptic segregation, we developed the PPSSI (Fig. 4d). Using DBSCAN [49] with a radius of 3 μm (details on Methods), we clustered synapses in each neuron and calculated the degree of segregation for each cluster (cPPSSI). We then multiplied the cPPSSI by the fraction of the synapse number and obtained the sum to determine the PPSSI of each neuron. Fig. 4b shows the result of applying PPSSI to 139,255 whole-brain neurons of FlyWire. The result showed a histogram resembling a normal distribution. When we created unsegregated ranking (details in Methods) by considering the number of synapses, APL and CT1 cells occupied the top 1–4 positions, indicating that we efficiently extracted unsegregated neurons (Fig. 4a, Ext.Data.Fig.4-3a). APL was also at the top for FlyEM (Ext.Data.Fig.4-1a). Similarly, we established segregated ranking and successfully extracted neurons with a high degree of segregation (Fig. 4c, Ext.Data.Fig.4-3; Ext.Data.Fig.4-1c and Ext.Data.Fig.4-4 for FlyEM).

Next, synapses with a cPPSSI between 0 and 0.1 were extracted, and the SC matrices (unsegregated synapses) of neurons and synapses were created. Synapses were then randomly sampled to generate 99 null SC matrices (random synapses), centered around the total number of connections (2,373,100) in the SC matrix (unsegregated synapses), forming a normal distribution (Fig. 4e, p=0.832, details in Methods). The FC-SC correlations of the SC matrices (unsegregated synapses) of neurons and synapses were significantly higher than those of the randomly extracted samples (Fig. 4e, p=0, 6.5e-43; Ext.Data.Fig.4-1d for FlyEM). Therefore, unsegregated synapses might strongly contribute to FC. A similar analysis was performed on synapses with a cPPSSI of 0.9–1, which surprisingly showed a significantly lower FC-SC correlation (Fig. 4f, p=9.2e-14, 0; Ext.Data.Fig.4-1e for FlyEM). Therefore, segregated synapses may not be able to contribute to strongly to the FC, and these findings are further explored in the Discussion section.

Among unsegregated synapses, reciprocal synapses have been well studied [31, 32, 33, 34, 35] and their function is considered to be clear (Fig. 4g, Ext.Data.Fig.4-1f). The shortest distance of such reciprocal synapses was extracted from whole-brain neurons, shown in Fig. 4h (Ext.Data.Fig.4-1g for FlyEM). They are particularly abundant within 2 μm (Ext.Data.Fig.4-2a,c for CT1 and APL cells), and acetylcholine and GABA constitute the majority (Fig. 4h). The comparison of the SC matrix based on reciprocal synapses (<2 μm) with the null SC matrices showed that the FC-SC correlation was significantly higher (Fig. 4I, p=0, 2.7e-32; Ext.Data.Fig.4-1h for FlyEM). Therefore, unsegregated synapses and reciprocal synapses (<2 μm) strongly contributed to FC. Furthermore, since the FC was the average of eight flies, such synapses are likely functionally common among individuals.

Region suppression analysis during fly walking

The whole-brain calcium imaging dataset from Brezovec et al. [14] provides fly walking data. Since fMRI pre-processing methods can be applied to calcium imaging data, we investigated whether voxel-level analysis using a general linear model (GLM) [50] could be applied to the fly walking task (Fig. 5a,

details in Methods). Fig. 5b shows the GLM analysis result. Similar to the results of Brezovec et al., our findings revealed that LAL, FB, and IPS neuropils showed strong activity; the GNG neuropil, which is highly connected to leg neuropils in the ventral nerve code [51], also exhibited strong activity. Although Brezovec et al. detected voxels that are strongly correlated with velocity, the GLM extracted voxels associated with walking behavior. Conversely, we found inactivity or strong suppression in the Wedge and AVLP neuropils. We searched for a GABA neuron that would fit with this phenomenon and managed to find one that extended its dendrites widely from the Wedge to AVLP neuropils (Fig. 5e, h). The synapse point cloud could also fit in this region (Fig. 5c). We called this neuron the Wedge-AVLP GABA neuron (WAGN). The Wedge neuropil receives mechanosensory (wind, sound) input and connects to WPNb neurons (Ext.Data.Fig.5-1a,b), which then connect to ER1 ring neurons that act as the fly's compass [52, 53]. Interestingly, the left WAGN was strongly interconnected with WPNb tier 2/3 [54] and received input from 22 ascending neurons (ANs; Fig. 5d). Therefore, it may be a pathway that provides walking behavior feedback to the compass; however, wind caused by walking was absent in the experimental setup (the fly was fixed and walked on a treadmill), and may relate to the strong regional suppression that was observed. As such, further experimentation is needed to pursue this topic.

The left WAGN resembles a hub neuron; however, like CT1 and APL cells, it has highly unsegregated synapses (PPSSI=0.133). Synapses on the medial side were highly segregated, but the lateral side was well unsegregated (Fig. 5h). It received input from ANs (212 synapses) mainly on the ventral side, and outputs to WPNb (65 synapses), widely from the medial to the lateral side (Fig. 5e). A histogram of the shortest straight-line distances between pre-synapses to WPNb and post-synapses from ANs is shown in Fig. 5f, and the closest distance was 852.3 nm (Fig. 5g). Many acetylcholine inputs (disynaptic inhibition [25]) were closer than this value (Fig. 5i), and many GABA inputs from ANs (Fig. 5f) further suppress such disynaptic inhibition. AVLP ventral suppression (Fig. 5b white arrows) may be the suppression from these ANs. Thus, a highly delicate and localized control is possibly exercised from WAGN to WPNb tier 2/3.

Discussion

Although nuisance factor removal methods such as global mean (GM) and aCompCor [42] are optimal for fMRI [10], calcium imaging showed different results. GM is the average of all voxels, and the regression of this signal is useful in fMRI because noise from the equipment and coils affects the entire voxel image. Conversely, in two-photon microscopy, noise does not affect all voxels because of the excitation of specific molecules by laser absorption, and GM does not show a positive effect. aCompCor extracts the component time-series from the voxel time-series of white matter and cerebrospinal fluid (CSF) via PCA and then performs a regression. In flies, the CSF had no ROI mask, but fibers had ROIs; therefore, fibers were used instead of the white matter. However, many synapses may exist around these fibers, and aCompCor was not as effective as in humans. Conversely, polynomial detrending [41] was highly effective (Fig. 1d-f), likely because of linear thermal noise and other factors caused by the continuous excitation of molecules (for 30 min). tCompCor [42] is the component time-series extracted by PCA from voxels with the top 1000 standard deviations among all voxels. It potentially captures minute fluctuations caused by fly movements and effectively removes them.

The SC matrix from a cPPSSI of 0.9–1 synapses resulted in a significantly lower FC-SC correlation than the SC matrix from randomly selected synapses (Fig. 4f for FlyWire, Ext.Data.Fig.4-1e for FlyEM). This result was surprising, but we propose several possible reasons. Neurons with highly segregated synapses include ascending neurons (ANs) and descending neurons (DNs), (Ext.Data.Fig.4-3b). They also have a small number of unsegregated synapses (i.e. Sep rank9: PPSSI=0.959, Sep rank11: PPSSI=0.964). They are thought to be specialized for input or output in the CNS regions and may show large differences between SC and FC. Another reason is that these neurons may have widespread logical OR inputs and outputs. In Fig. 4c, an action potential at one point in the input synapse (blue) is likely transmitted to all red synapses. Such an OR circuit-like disproportionate input–output possibly causes a mismatch with the FC, because the functional activity in the output region originates from activity at a single location. These neurons are likely those whose FC are difficult to capture. Conversely, neurons with highly unsegregated

synapses may capture the inputs of neighboring synapses, such as forming a logical AND circuit, correlating well with the output regions.

The FC-SC correlation was highly dependent on ROI count in both flies and humans (Fig. 2d). Through optimal nuisance factor removal and smoothing, we achieved r=0.87 at 20 ROIs. Furthermore, by applying Spearman correlation instead of Pearson, we obtained r=0.928. Thus, for a reasonably small ROI count the correlation was very high; however, for 10,000 ROIs, the correlation decreased to r=0.57. This phenomenon could be attributed to the presence of highly segregated synapses. Such neurons are widespread in the CNS (Fig. 4b, Ext.Data.Fig.4-2f) and are thought to provide logical OR circuits. When ROI volume was large (when the ROI count was small), a single ROI could cover the distributed input synapses. However, when a ROI was divided, input synapses were also divided across many ROIs, and the mismatch between SC and FC would increase. Other possibilities include the presence of gap junctions and FC due to neuropeptides [55], but they are outside of the scope of the present study and their relationship with ROI count is unclear.

In this study, we applied fMRI techniques directly to calcium imaging in flies and found many similarities between humans and flies (Fig. 2d). The calcium signal represents pre-synaptic population dynamics and likely includes the localized functional activity of unsegregated synapses [25, 31, 32, 33, 34], such as non-spiking [21, 22, 23, 24, 25, 26] and sub-threshold neuronal activity [18]. For fMRI, the signal captures localized functional activity as blood-oxygenation-level-dependent signal via neuro vascular coupling [40]. These two signals can be pre-processed (Fig. 1, Fig. 2) and analyzed (Fig. 5a) in surprisingly similar ways. This is unlikely a coincidence, and it suggests that similar design concepts underlie neural circuits in flies and mammals. Using *D. melanogaster* as a model animal, we were able to elucidate detailed local functional activities around unsegregated synapses and compare these results to the brain activities of mammals, including humans.

Materials and Methods

Preprocessing of *D. melanogaster* calcium imaging data

Whole-brain calcium imaging data of *D. melanogaster* were acquired by Brezovec et al. [14] and downloaded from DANDI (https://dandiarchive.org/dandiset/000727/0.240106.0043). 4D NIfTI image data (256×128×49 voxels, 3384 frames) were extracted from a NWB file by an in-house MATLAB script. The FDA template, made from in-vivo calcium imaging, was resized (256×128×49 voxels, 2.45×2.28×3.72μm for a voxel) and used as a template because the original thresholded FDA template [56] was extremely large (1652×768×479 voxels), and the calcium imaging file was large (more than 40 GB); therefore, a smaller template with the imaging data was preferably used. Preprocessing and image registration were performed using Statistical Parametric Mapping (SPM12) [57] and ANTs [58] (Ext.Data.Fig.1-1a). Motion and slice timing correction were performed using SPM12, and the averaged NIfTI image was registered by ANTs to the resized FDA template. Lastly, 4D NIfTI images were transformed using the transform information. The data contained n=9 flies, but 8 flies were used for the ROI-based analysis because of missing time-series in some ROIs in one fly. Nine flies were used in the GLM analysis.

Combinations of the following nuisance factor removal methods were investigated: global mean (average signal across all voxels), global signal (average signal across all brain voxels), mean white matter (average signal across fiber voxels), 6HMP (head motion parameters), 24HMP, aCompCor, tCompCor [42], and polynomial detrending (Poly) [41]. These methods were implemented by an in-house MATLAB script [59]. A full width at half maximum (FWHM) from 1 voxel (2.28 μm) to 30 voxels (68.4 μm), at a 1 voxel step, was investigated to determine the optimal spatial smoothing size for calcium imaging data. Temporal high-pass filters were also examined from 0.1 Hz to 0.001 Hz.

Transformation of EM connectome data into the resized FDA template

In the FlyWire case, connectome data, such as neurons and synapses, were downloaded from FlyWire Codex (https://codex.flywire.ai/) and Zenodo (https://zenodo.org/records/10676866) [13, 60, 45]. Detailed synapse data were saved in an Apache feather format, which was then converted to a CSV file. Synapse points were transformed from the FlyWire space to a JRC2018 female template [61] by the Python navis-flybrains package [61]. Since FlyWire coordinates are left and right reversed [13], they were flipped on the JRC2018 female template, and these points were transformed to the resized FDA template by ANTs. The use of these two templates facilitated precise data alignment across different modalities.

In the FlyEM case, the latest connectome data were downloaded from Janelia's DVID website (https://dvid.io/blog/release-v1.2/). Like those in the FlyWire case, synapse points were transformed from the FlyEM space to a JRC2018 female template by the Python navis-flybrains package. These points were transformed to a resized FDA template by ANTs.

Generation of regions of interest for the hemibrain

The hemibrain neuropil atlas (114 ROIs, including primary and sub-regions, aligned with the FlyEM space) was downloaded from Virtual Fly Brain (https://www.virtualflybrain.org/). ROI files were transformed from the FlyEM space to a JRC2018 female template by Java template-building scripts (https://github.com/saalfeldlab/template-building) [61]. They were transformed to a resized FDA template by ANTs. In Fig. 3, 63 primary ROIs mentioned above were used. The 52 ROIs in Fig. 1 were selected from the primary ROIs, and approximately 50 ROIs (those used by Turner et al. [9]) were selected. ROIs were segmented by SCKm (Fig. 1 and Fig. 2) via the k-means clustering of the SC matrix of 146,604 voxels in the hemibrain. They were also segmented by DistKm (Fig. 1 and Fig. 2) via the k-means clustering of the distance of 146,604 voxels in the hemibrain.

The SC matrix was calculated according to synapse locations and ROIs. Since synapse data formats differ between FlyEM and FlyWire, they were standardized by using post-synapses within ROIs. The input and output neurons at each ROI were extracted from the paired pre- and post-synapse data. Then the input and

output neurons and their synapses that were common between ROI pairs were counted to create SC matrices for neurons and synapses. The FC matrix was calculated using the pre-processed voxel time-series and ROIs. The intensity of the voxels in the ROI was averaged to obtain the average intensity time-series of the ROI. Then, Pearson correlation was calculated between ROI pairs to generate the FC matrix. The correlation coefficients were z-transformed, calculated for eight flies, and then averaged to obtain the final FC matrix.

FC-SC detection and correlation

FC-SC correlation was calculated by taking the Pearson correlation between the logarithm of the SC matrix and the FC matrix, as done in other studies [6, 7, 10]. In the SC matrix, elements with zero connections become -*Inf* when logarithmically converted, so we substituted zero for them. Also, the diagonal elements of the FC matrix become *Inf* when z-transformed, so we replaced them with the maximum value of the matrix. For one FC matrix, we calculated its correlation with both the neuron SC matrix and the synapse SC matrix. FC-SC detection was calculated by ROC (Receiver Operating Characteristic) curve analysis. This gives the detection accuracy of the FC matrix when the SC matrix is used as ground truth. Thresholds were taken from 0% to 99% by 1% steps of all elements of the SC matrix, and 100 AUCs (Area Under the Curve) were calculated. The average of these AUCs is called the FC-SC detection. FC-SC correlation indicates the similarity of the two matrices, while FC-SC detection indicates the detection accuracy. Although the digit number of connections differs between neurons and synapses, FC-SC detection can absorb such differences. The FC-SC detection & correlation score was calculated as follows:

$$FC\text{-}SC_{det\&corr\ score} = |FC\text{-}SC_{correlation}| + 2 \times |FC\text{-}SC_{detection} - 0.5| \#(1)$$

The FC-SC detection & correlation score is in the range of [0 2], where the larger the score, the higher the similarity and detection accuracy.

PPSSI

The PPSSI (Fig. 4d) was used in DBSCAN [49] with a radius of 3 μm to generate pre- and post-synaptic clusters. The radius was empirically defined by several criteria. Firstly, CT1 and APL cells have the shortest distance of reciprocal synapses, within 2 μm (Ext.Data.Fig.4-2a,c). In zebrafish, reciprocal synapses were defined within 2.5 μm [35]. Schneider-Mizell et al. [19] defined a twig as a branch within 3 μm from the backbone of the cytoskeleton, and 80% of synaptic inputs in motor neurons are in the twig. In addition, 97% of pre-synaptic sites are located at less than 3 μm from the mitochondria. Therefore, 3 μm was deemed appropriate for the synapse cluster radius. Once the synapse clusters were determined by DBSCAN, the degree of synaptic segregation for each cluster was calculated using the following formula:

$$cPPSSI_i = \left(\frac{pre_i - post_i}{pre_i + post_i}\right)^2, \#(2)$$

where pre_i and $post_i$ are the pre- and post-synapse counts in cluster *i*, respectively. The cPPSSI of each cluster (each synapse) is in the range of [0 1]. The PPSSI of each neuron was calculated as follows:

$$PPSSI = \sum_{i=1}^{N} \frac{(pre_i + post_i)}{W} \cdot cPPSSI_i \#(3)$$

where N is the cluster number, and W is the total synapse count for a neuron.

The unsegregated ranking was calculated based on the PPSSI and total synapse count of neuron k:

$$unsegregated\ score_k = log_{10}(W_k) \cdot (1 - PPSSI_k)\#(4)$$

where $PPSSI_k$ is the PPSSI of neuron k and W_k is the total synapse count of neuron k. This allows us to extract neurons with many inputs and outputs and highly unsegregated synapses. The segregated ranking was also calculated in the same way, using the following score:

$$segregated\ score_k = log_{10}(W_k) \cdot PPSSI_k\#(5)$$

A similar index to our PPSSI, namely, the segregation index, has been defined in the literature [19], but its use poses several problems. For neurons such as ANs and DNs, that have only input or output synapses, the segregation index results in calculations of $0 \times \infty$ or division by 0; consequently, calculation becomes impossible. Despite the [0 1] range of indices, the histogram is heavily biased toward 0 because of the use of the logarithm, and the mean is much closer to 0 than 0.5 (Ext.Data.Fig.4-1i, j).

Therefore, in the present study, we developed the more robust PPSSI because it is less biased and its mean is close to 0.5 (Fig. 4b, Ext.Data.Fig.4-1b).

GLM Analysis for the fly walking task

GLM analysis (Fig. 5a) was performed to investigate the whole-brain functional activity during the fly walking task. Movement velocity data were extracted from an NWB file by an in-house MATLAB script. Walking was defined as 1σ (34%) or more of the movement velocity and divided into walking and other. Less than 10% of movement velocity was zero cut. The canonical calcium response function (CRF) was created by the gamma probability density function (a=1.7, b=0.25) in MATLAB based on the GCaMP6f response [62]. The walking-task time-series was transformed into a calcium response time-series by convolution with the CRF. GLM design matrices were created using the calcium response time-series and nuisance factors (polynomial detrending and tCompCor). In whole-brain voxels, smoothing was applied with a kernel radius of 8 voxels (18.24 μm). Then, a Tukey taper (taper size = 8) was used for GLM pre-whitening [63]. A mixed-effects model [43] was used for group analysis, and the t-value of each voxel was calculated via the second-level analysis of OLS regression with a Tukey taper. These analyses were implemented using in-house MATLAB scripts [64].

Statistical Analysis

A Mann–Whitney U test was used to examine whether the combination of spatial smoothing and nuisance factor removal was effective. Statistical significance was set at $p<0.05$, and Bonferroni correction was applied to correct the familywise error (FWE) rate. A permutation test was performed to analyze whether specific synapses (segregated, unsegregated, or reciprocal synapses) affect SC-FC correlation. The SC matrix (specific synapses) in the 63 ROIs in the hemibrain was generated, and its SC-FC correlation was calculated. Then, 99 null SC matrices (random synapses) were generated so that they would be normally distributed around the total number of connections in the SC matrix (specific synapses). Since the SC-FC correlations of the null SC matrices (random synapses) also roughly followed a normal distribution, the

T-value of the SC-FC correlation of the SC matrix (specific synapses) was calculated using the cumulative distribution function of the normal distribution. For GLM analysis, a mixed-effects model was used for group analysis.

Acknowledgements

The authors wish to thank Dr. Clandinin for providing valuable calcium imaging data and answering our question.

This research was supported by the program for Brain Mapping by Integrated Neurotechnologies for Disease Studies (Brain/MINDS 2.0) from the Japan Agency for Medical Research and Development, AMED. Grant number: JP24wm0625408.

References

[1] G. L. Gerstein and D. H. Perkel, "Simultaneously recorded trains of action potentials: Analysis and functional interpretation.," *Science*, vol. 164, pp. 828-830, 1969.

[2] G. L. Gerstein, P. Bedenbaugh and A. M. Aertsen, "Neuronal assemblies," *IEEE Trans. Biomed. Eng.*, vol. 36, pp. 4-14, 1989.

[3] K. J. Friston, C. D. Frith, P. F. Liddle and R. S. Franckowiak, "Functional Connectivity: The Principal-Component Analysis of Large (PET) Data Sets," *J. Cereb. Blood Flow Metab.*, vol. 13, pp. 5-14, 1993.

[4] K. Friston, R. Moran and A. K. Seth, "Analysing connectivity with Granger causality and dynamic causal modelling," *Curr. Op. in Neuro.*, vol. 23, no. 2, pp. 172-178, 2013.

[5] P. Hagmann, L. Cammoun, X. Gigandet, R. Meuli, C. J. Honey, V. J. Wedeen and O. Sporns, "Mapping the Structural Core of Human Cerebral Cortex," *PLoS Biol*, vol. 6, no. 7, p. e159, 2008.

[6] C. J. Honey, O. Sporns, L. Cammoun, X. Gigandet, J. P. Thiran, R. Meuli and P. Hagmann, "Predicting human resting-state functional connectivity from structural connectivity," *Proc. Natl. Acad. Sci. USA*, vol. 106, no. 6, pp. 2035-2040, 2009.

[7] C. J. Honey, J.-P. Thivierge and O. Sporns, "Can structure predict function in the human brain?," *NeuroImage,* vol. 52, no. 3, pp. 766-776, 2010.

[8] G. L. Baum, Z. Cui, D. R. Roalf, R. Ciric, R. F. Betzel, B. Larsen, M. Cieslak, P. A. Cook, C. H. Xia, T. M. Moore, K. Ruparel, D. J. Oathes, A. F. Alexander-Bloch, R. T. Shinohara, A. Raznahan, R. E. Gur, R. C. Gur, D. S. Bassett and T. D. Satterthwaite, "Development of structure–function coupling in human brain networks during youth," *PNAS,* vol. 117, no. 1, pp. 771-778, 2020.

[9] M. H. Turner, K. Mann and T. R. Clandinin, "The connectome predicts resting-state functional connectivity across the Drosophila brain," *Current Biology,* vol. 31, p. 2386–2394, 2021.

[10] T. Okuno, J. Hata, C. Kawai, H. Okano and A. Woodward, "A Novel Directed Seed-Based Connectivity Analysis Toolbox Applied to Human and Marmoset Resting-State fMRI," *J. Neurosci.,* vol. 44, no. 45, p. e0389242024, 2024.

[11] R. Hira, L. B. Townsend, I. T. Smith, C.-H. Yu, J. N. Stirman, Y. Yu and S. L. Smith, "Mesoscale functional architecture in medial posterior parietal cortex," *eLife,* p. 105213v1, 2025.

[12] L. K. Scheffer, C. S. Xu, M. Januszewski, Z. Lu, S. Takemura, K. J. Hayworth, G. B. Huang, K. Shinomiya, J. Maitlin-Shepard, S. Berg, J. Clements, P. M. Hubbard, W. T. Katz, L. Umayam, T. Zhao, D. Ackerman, T. Blakely, J. Bogovic, T. Dolafi, D. Kainmueller, T. Kawase, K. A. Khairy, L. Leavitt, P. H. Li, L. Lindsey, N. Neubarth, D. J. Olbris, H. Otsuna, E. T. Trautman, M. Ito, A. S. Bates, J. Goldammer, T. Wolff, R. Svirskas, P. Schlegel, E. Neace, C. J. Knecht, C. X. Alvarado, D. A. Bailey, S. Ballinger, J. Z. Borycz, B. S. Canino, N. Cheatham, M. Cook, M. Dreher, O. Duclos, B. Eubanks, K. Fairbanks, S. Finley, N. Forknall, A. Francis, G. P. Hopkins, E. M. Joyce, S. Kim, N. A. Kirk, J. Kovalyak, S. A. Lauchie, A. Lohff, C. Maldonado, E. A. Manley, S. McLin, C. Mooney, M. Ndama, O. Ogundeyi, N. Okeoma, C. Ordish, N. Padilla, C. M. Patrick, T. Paterson, E. E. Phillips, E. M. Phillips, N. Rampally, C. Ribeiro, M. K. Robertson, J. M. Rymer, S. M. Ryan, M. Sammons, A. K. Scott, A. L. Scott, A. Shinomiya, C. Smith, K. Smith, N. L. Smith, M. A. Sobeski, A. Suleiman, J. Swift, S. Takemura, I. Talebi, D. Tarnogorska, E. Tenshaw, T. Tokhi, J. J. Walsh, T. Yang, J. A. Horne, F. Li, R. Parekh, P. K. Rivlin, V. Jayaraman, M. Costa, G. S. Jefferis, K. Ito, S. Saalfeld, R. George, I. A. Meinertzhagen, G. M. Rubin, H. F. Hess, V. Jain and S. M. Plaza, "A connectome and analysis of the adult Drosophila central brain," *eLife,* vol. 9, p. e57443, 2020.

[13] S. Dorkenwald, A. Matsliah, A. R. Sterling, P. Schlegel, S. Yu, C. E. McKellar, A. Lin, M. Costa, K. Eichler, Y. Yin, W. Silversmith, C. Schneider-Mizell, C. S. Jordan, D. Brittain, A. Halageri, K. Kuehner, O. Ogedengbe, R. Morey, J. Gager, K. Kruk, E. Perlman, R. Yang, D. Deutsch, D. Bland, M. Sorek, R. Lu, T. Macrina, K. Lee, J. A. Bae, S. Mu, B. Nehoran, E.

Mitchell, S. Popovych, J. Wu, Z. Jia, M. A. Castro, N. Kemnitz, D. Ih, A. S. Bates, N. Eckstein, J. Funke, F. Collman, D. D. Bock, G. S. Jefferis, H. S. Seung, M. Murthy and The FlyWire Consortium, "Neuronal wiring diagram of an adult brain," *Nature,* vol. 634, p. 124–138, 2024.

[14] B. E. Brezovec, A. B. Berger, Y. A. Hao, F. Chen, S. Druckmann and T. R. Clandinin, "Mapping the neural dynamics of locomotion across the Drosophila brain," *Current Biology,* vol. 34, p. 710–726, 2024.

[15] P. Schlegel, A. S. Bates, T. Stürner, S. R. Jagannathan, N. Drummond, J. Hsu, L. S. Capdevila, A. Javier, E. C. Marin, A. Barth-Maron, I. F. Tamimi, F. Li, G. M. Rubin, S. M. Plaza, M. Costa and G. S. Jefferis, "Information flow, cell types and stereotypy in a full olfactory connectome," *eLife,* vol. 10, p. e66018, 2021.

[16] P. Schlegel, Y. Yin, A. S. Bates, S. Dorkenwald, K. Eichler, P. Brooks, D. S. Han, M. Gkantia, M. D. Santos, E. J. Munnelly, G. Badalamente, L. S. Capdevila, V. A. Sane, A. M. Fragniere, L. Kiassat, M. W. Pleijzier, T. Stürner, I. F. Tamimi, C. R. Dunne, I. Salgarella, A. Javier, S. Fang, E. Perlman, T. Kazimiers, S. R. Jagannathan, A. Matsliah, A. R. Sterling, S. Yu, C. E. McKellar, FlyWire Consortium, M. Costa, H. S. Seung, M. Murthy, V. Hartenstein, D. D. Bock and G. S. Jefferis, "Whole-brain annotation and multi-connectome cell typing of Drosophila," *Nature,* vol. 634, pp. 139-152, 2024.

[17] L. Heinrich, J. Funke, C. Pape, J. Nunez-lglesias and S. Saalfeld, "Synaptic Cleft Segmentation in Non-Isotropic Volume Electron Microscopy of the Complete Drosophila Brain," *arXiv,* p. 1805.02718, 2018.

[18] T. Branco and M. Häusser, "The single dendritic branch as a fundamental functional unit in the nervous system," *Current Opinion in Neurobiology,* vol. 20, pp. 494-502, 2010.

[19] C. M. Schneider-Mizell, S. Gerhard, M. Longair, T. Kazimiers, F. Li, M. F. Zwart, A. Champion, F. M. Midgley, R. D. Fetter, S. Saalfeld and A. Cardona, "Quantitative neuroanatomy for connectomics in Drosophila," *eLife,* vol. 5, p. e12059, 2016.

[20] O. T. Shafer, G. J. Gutierrez, K. Li, A. Mildenhall, D. Spire, J. Marty, A. A. Lazar and M. D. Fernandez, "Connectomic analysis of the Drosophila lateral neuron clock cells reveals the synaptic basis of functional pacemaker classes," *eLife,* vol. 11, p. e79139, 2022.

[21] M. Meier and A. Borst, "Extreme Compartmentalization in a Drosophila Amacrine Cell," *Current Biology,* vol. 29, pp. 1545-1550, 2019.

[22] R. Behnia, D. A. Clark, A. G. Carter, T. R. Clandinin and C. Desplan, "Processing properties of ON and OFF pathways for Drosophila motion detection," *Nature,* vol. 512, pp.

427-430, 2014.

[23] E. Gruntman, P. Reimers, S. Romani and M. B. Reiser, "Non-preferred contrast responses in the Drosophila motion pathways reveal a receptive field structure that explains a common visual illusion," *Current Biology,* vol. 31, pp. 5286-5298, 2021.

[24] L. N. Groschner, J. G. Malis, B. Zuidinga and A. Borst, "A biophysical account of multiplication by a single neuron," *Nature,* vol. 603, pp. 119-123, 2022.

[25] A. Braun, A. Borst and M. Meier, "Disynaptic inhibition shapes tuning of OFF-motion detectors in Drosophila," *Current Biology,* vol. 33, pp. 2260-2269, 2023.

[26] J. E. Schenk and Q. Gaudry, "Nonspiking Interneurons in the Drosophila Antennal Lobe Exhibit Spatially Restricted Activity," *eNeuro,* vol. 10, no. 1, pp. ENEURO.0109-22.2022, 2023.

[27] K. Inada, Y. Tsuchimoto and H. Kazama, "Origins of Cell-Type-Specific Olfactory Processing in the Drosophila Mushroom Body Circuit," *Neuron,* vol. 95, pp. 357-367, 2017.

[28] H. Amin, A. A. Apostolopoulou, R. Suárez-Grimalt, E. Vrontou and A. C. Lin, "Localized inhibition in the Drosophila mushroom body," *eLife,* vol. 9, p. e56954, 2020.

[29] X. Liu and R. L. Davis, "The GABAergic anterior paired lateral neuron suppresses and is suppressed by olfactory learning," *Net. Neurosci.,* vol. 12, pp. 53-59, 2009.

[30] A. Lin, R. Yang, S. Dorkenwald, A. Matsliah, A. R. Sterling, P. Schlegel, S. Yu, C. E. McKellar, M. Costa, K. Eichler, A. S. Bates, N. Eckstein, J. Funke, G. S. Jefferis and M. Murthy, "Network statistics of the whole-brain connectome of Drosophila," *Nature,* vol. 634, pp. 153-165, 2024.

[31] W. N. Grimes, W. Li, A. E. Chávez and J. S. Diamond, "BK channels modulate pre- and postsynaptic signaling at reciprocal synapses in retina," *Nat. Neurosci.,* vol. 12, no. 5, pp. 585-592, 2009.

[32] W. N. Grimes, J. Zhang, C. W. Graydon, B. Kachar and J. S. Diamond, "Retinal Parallel Processors: More than 100 Independent Microcircuits Operate within a Single Interneuron," *Neuron,* vol. 65, pp. 873-885, 2010.

[33] I. Cervantes-Sandoval, A. Phan, M. Chakraborty and R. L. Davis, "Reciprocal synapses between mushroom body and dopamine neurons form a positive feedback loop required for

learning," *eLife,* vol. 6, p. e23789, 2017.

[34] S. Takumura, Y. Aso, T. Hige, A. Wong, Z. Lu, C. S. Xu, P. K. Rivlin, H. Hess, T. Zhao, T. Parag, S. Berg, G. Huang, W. Katz, D. J. Olbris, S. Plaza, L. Umayam, R. Aniceto, L. Chang, S. Lauchie, O. Ogundeyi, C. Ordish, A. Shinomiya, C. Sigmund, S. Takemura, J. Tran, G. C. Turner, G. M. Rubin and L. K. Scheffer, "A connectome of a learning and memory center in the adult Drosophila brain," *eLife,* vol. 6, p. e23789, 2017.

[35] A. A. Wanner, C. Genoud, T. Masudi, L. Siksou and R. W. Friedrich, "Dense EM-based reconstruction of the interglomerular projectome in the zebrafish olfactory bulb," *Nat. Neurosci.,* vol. 19, pp. 816-825, 2016.

[36] T. Euler, P. B. Detwiler and W. Denk, "Directionally selective calcium signals in dendrites of starburst amacrine cells," *Nature,* vol. 418, pp. 845-852, 2002.

[37] J. C. Patel, P. Witkovsky, M. V. Avshalumov and M. E. Rice, "Mobilization of Calcium from Intracellular Stores Facilitates Somatodendritic Dopamine Release," *J. Neurosci.,* vol. 29, no. 20, pp. 6568-6579, 2009.

[38] C. Grienberger, X. Chen and A. Konnerth, "Dendritic function in vivo," *Trends Neurosci.,* vol. 38, no. 1, pp. 45-54, 2015.

[39] A. Shapson-Coe, M. Januszewski, D. R. Berger, A. Pope, Y. Wu, T. Blakely, R. L. Schalek, P. H. Li, S. Wang, J. Maitin-Shepard, N. Karlupia, S. Dorkenwald, E. Sjostedt, L. Leavitt, D. Lee, J. Troidl, F. Collman, L. Bailey, A. Fitzmaurice, R. Kar, B. Field, H. Wu, J. Wagner-Carena, D. Aley, J. Lau, Z. Lin, D. Wei, H. Pfister, A. Peleg, V. Jain and J. W. Lichtman, "A petavoxel fragment of human cerebral cortex reconstructed at nanoscale resolution," *Science,* vol. 384, p. eadk4858, 2024.

[40] C. Iadecola, "The Neurovascular Unit Coming of Age: A Journey through Neurovascular Coupling in Health and Disease," *Neuron,* vol. 1, no. 27, pp. 17-42, 2017.

[41] O. Friman, M. Borga, P. Lundberg and H. Knutsson, "Detection and detrending in fMRI data analysis," *NeuroImage,* vol. 22, pp. 645-655, 2004.

[42] Y. Behzadi, K. Restom, J. Liau and T. T. Liu, "A component based noise correction method (CompCor) for BOLD and perfusion based fMRI," *NeuroImage,* vol. 37, pp. 90-101, 2007.

[43] A. P. Holmes and K. J. Friston, "Generalisability, Random Effects & Population Inference," *NeuroImage,* vol. 7, no. 4, p. S754, 1998.

[44] P. Majka, S. Bai, S. Bakola, S. Bednarek, J. M. Chen, N. Jermakow, L. Passarelli, D. H. Reser, P. Theodoni, K. H. Worthy, X. Wang, D. K. Wojcik, P. P. Mitra and M. G. P. Rosa, "Open access resource for cellular-resolution analyses of corticocortical connectivity in the marmoset monkey," *Nat. Comm.,* vol. 11, p. 1133, 2020.

[45] N. Eckstein, A. S. Bates, A. Champion, M. Du, Y. Yin, P. Schlegel, A. K.-Y. Lu, T. Rymer, S. Finley-May, T. Paterson, R. Parekh, S. Dorkenwald, A. Matsliah, S.-C. Yu, C. McKellar, A. Sterling, K. Eichler, M. Costa, S. Seung, M. Murthy, V. Hartenstein, G. S. Jefferis and J. Funke, "Neurotransmitter classification from electron microscopy images at synaptic sites in Drosophila melanogaster," *Cell,* vol. 187, no. 10, pp. 2574-2594.e23, 2024.

[46] R. Tomioka, K. Okamoto, T. Furuta, F. Fujiyama, T. Iwasato, Y. Yanagawa, K. Obata, T. Kaneko and N. Tamamaki, "Demonstration of long-range GABAergic connections distributed throughout the mouse neocortex," *Eur. J. Neurosci.,* vol. 21, pp. 1587-1600, 2005.

[47] S. Higo, K. Akashi, K. Sakimura and N. Tamamaki, "Subtypes of GABAergic neurons project axons in the neocortex," *Front. Neuroanat.,* vol. 3, p. 25, 2009.

[48] C. Mazo, A. Nissant, S. Saha, E. Peroni, P.-M. Lledo and G. Lepousez, "Long-range GABAergic projections contribute to cortical feedback control of sensory processing," *Nat. Comm.,* vol. 13, p. 6879, 2022.

[49] M. Ester, H.-P. Kriegel, J. Sander and X. Xu, "A density-based algorithm for discovering clusters in large spatial databases with noise.," *KDD'96: Proceedings of the Second International Conference on Knowledge Discovery and Data Mini,* pp. 226-231, 1996.

[50] R. L. Buckner, J. R. Andrews-Hanna and D. L. Schacter, "The Brain's Default Network Anatomy, Function, and Relevance to Disease," *Ann. N.Y. Acad. Sci.,* vol. 1124, pp. 1-38, 2008.

[51] S. Namiki, M. H. Dickinson, A. M. Wong, W. Korff and G. M. Card, "The functional organization of descending sensory-motor pathways in Drosophila," *eLife,* vol. 7, p. e34272, 2018.

[52] T. S. Okubo, P. Patella, I. D'Alessandro and R. I. Wilson, "A Neural Network for Wind-Guided Compass Navigation," *Neuron,* vol. 107, pp. 924-940, 2020.

[53] B. El Jundi and M. Dacke, "Insect Orientation: The Drosophila Wind Compass Pathway," *Current Biology,* vol. 31, no. 2, pp. PR83-R85, 2021.

[54] K. E. Coates, S. A. Calle-Schuler, L. M. Helmick, V. L. Knotts, B. N. Martik, F. Salman, L. T. Warner, S. V. Valla, D. D. Bock and A. M. Dacks, "The Wiring Logic of an Identified Serotonergic Neuron That Spans Sensory Networks," *J. Neurosci.*, vol. 40, no. 33, pp. 6309-6327, 2020.

[55] F. Randi, A. K. Sharma, S. Dvali and A. M. Leifer, "Neural signal propagation atlas of Caenorhabditis elegans," *Nature*, vol. 623, pp. 406-414, 2023.

[56] B. E. Brezovec, A. B. Berger, Y. A. Hao, A. Lin, O. M. Ahmed, D. A. Pacheco, S. Y. Thiberge, M. Murthy and T. R. Clandinin, "BIFROST: A method for registering diverse imaging datasets of the Drosophila brain," *Proc Natl Acad Sci USA*, vol. 121, no. 47, p. e2322687121, 2024.

[57] W. Penny, K. Friston, J. Ashburner, S. Kiebel and T. Nichols, Statistical Parametric Mapping: The Analysis of Functional Brain Images, London: Elsevier, 2007.

[58] B. B. Avants, N. J. Tustison, G. Song, P. A. Cook, A. Klein and J. C. Gee, "A reproducible evaluation of ANTs similarity metric performance in brain image registration," *NeuroImage*, vol. 54, no. 3, pp. 2033-2044, 2011.

[59] T. Okuno and A. Woodward, "Vector Auto-Regressive Deep Neural Network: A Data-Driven Deep Learning-Based Directed Functional Connectivity Estimation Toolbox," *Front. Neurosci.*, vol. 15, p. 764796, 2021.

[60] J. Buhmann, A. Sheridan, C. Malin-Mayor, P. Schlegel, S. Gerhard, T. Kazimiers, R. Krause, T. M. Nguyen, L. Heinrich, W.-C. A. Lee, R. Wilson, S. Saalfeld, G. S. Jefferis, D. D. Bock, S. C. Turaga, M. Cook and J. Funke, "Automatic detection of synaptic partners in a whole-brain Drosophila electron microscopy data set," *Nature Methods*, vol. 18, pp. 771-774, 2021.

[61] J. A. Bogovic, H. Otsuna, L. Heinrich, M. Ito, J. Jeter, G. Meissner, A. Nern, J. Colonell, O. Malkesman, K. Ito and S. Saalfeld, "An unbiased template of the Drosophila brain and ventral nerve cord," *PLoS ONE*, vol. 15, no. 12, p. e0236495, 2020.

[62] T.-W. Chen, T. J. Wardill, Y. Sun, S. R. Pulver, S. L. Renninger, A. Baohan, E. R. Schreiter, R. A. Kerr, M. B. Orger, V. Jayaraman, L. L. Looger, K. Svoboda and D. S. Kim, "Ultrasensitive fluorescent proteins for imaging neuronal activity," *Nature*, vol. 499, pp. 295-300, 2013.

[63] M. W. Woolrich, B. D. Ripley, M. Brady and S. M. Smith, "Temporal Autocorrelation in

Univariate Linear Modeling of FMRI Data," *NeuroImage,* vol. 14, pp. 1370-1386, 2001.

[64] T. Okuno, N. Ichinohe and A. Woodward, "A reappraisal of the default mode and frontoparietal networks in the common marmoset brain," *Front. Neuroimaging,* vol. 2, p. 1345643, 2024.

Figures

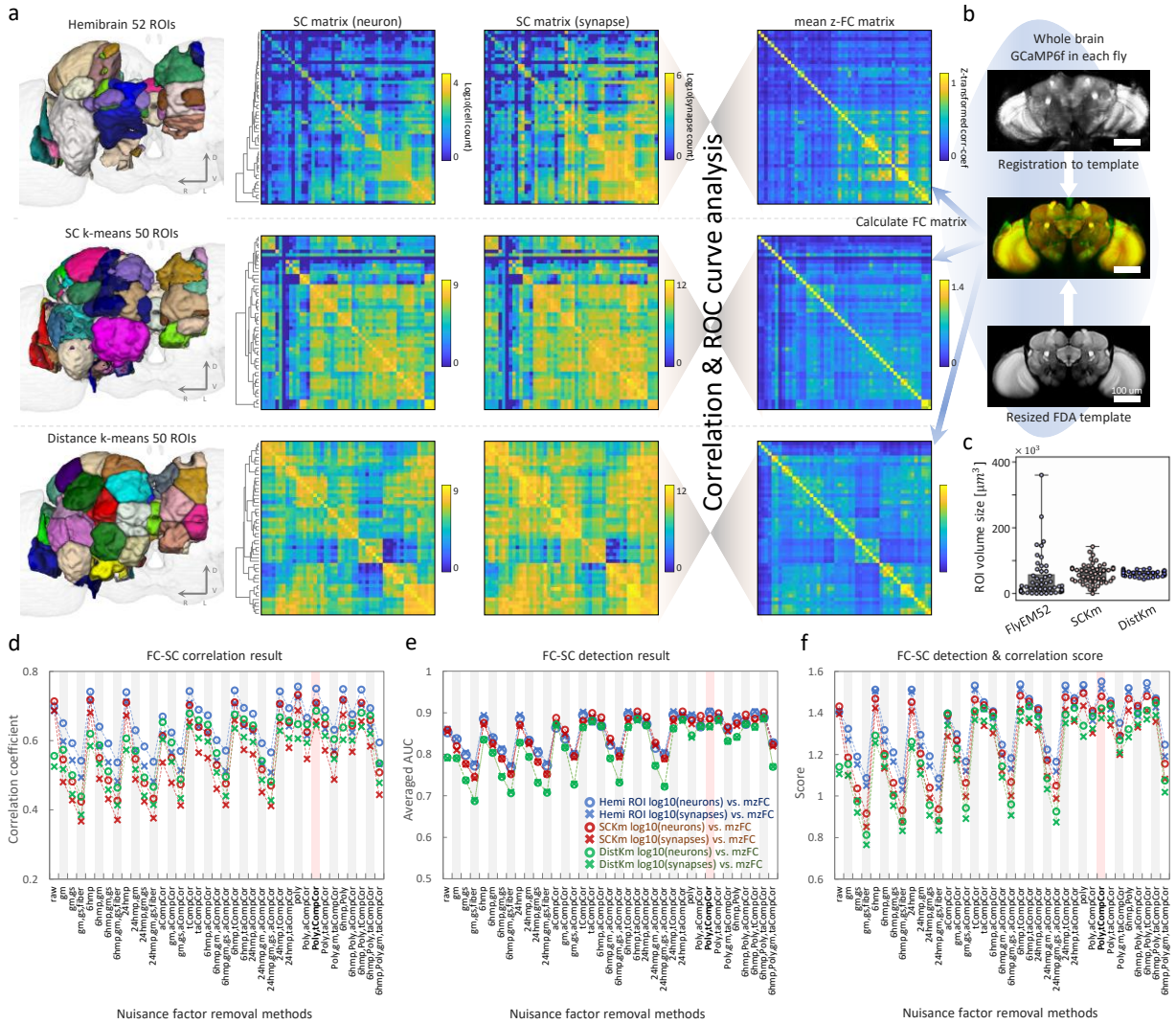

Fig. 1 Comparison between SC and FC, and optimal nuisance factor removal methods. a, Schematic image of the comparison between SC matrices and FC matrices. (left) Three ROI types: Hemibrain anatomical 52 ROIs, SCKm 50 ROIs, and DistKm 50 ROIs. (center) SC matrices (neuron) and SC matrices (synapse) for each ROI type. (right) FC matrices for an average of 8 flies for each ROI type. **b,** Schematic image of calcium imaging data registration. **c,** Swarm plot of ROI volume for each ROI type. **d,** Results of nuisance factor removal method investigation. The vertical axis shows the correlation coefficient, and the horizontal axis shows the FC-SC correlation for each method. Results are plotted for the three ROI types. **e,** The vertical axis shows the averaged AUC of 100 thresholds, and the horizontal axis is the same as **d**. **f,** The vertical axis shows the FC-SC detection & correlation score, and the horizontal axis is the same as **d**.

399

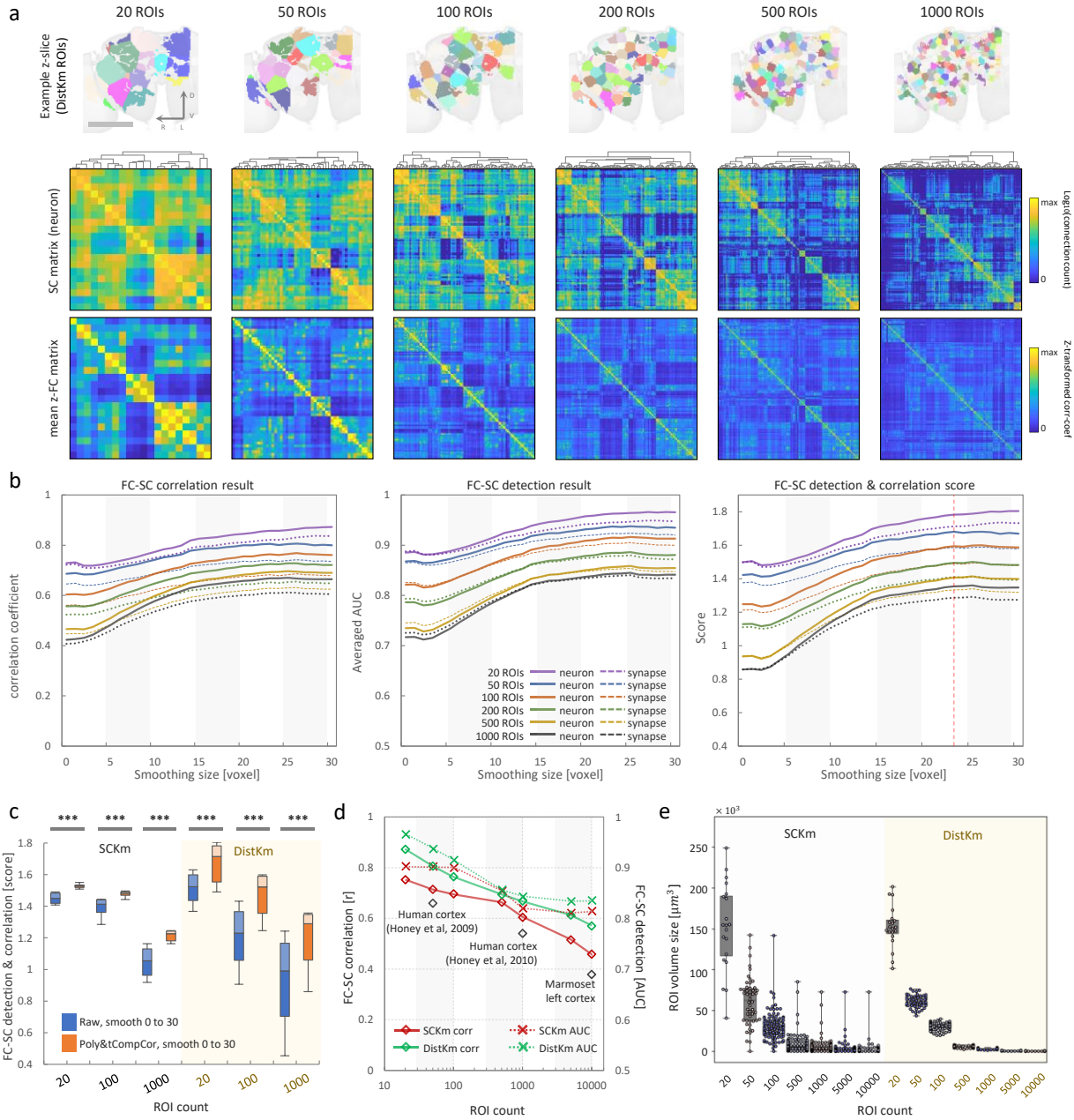

Fig. 2 Investigating spatial smoothing size, and comparison of FC-SC correlation between mammals and flies. a, (top) Example z-slice of the reduced FDA template with DistKm ROIs from 20 to 1000 ROIs. (middle) SC matrices (neuron) of DistKm ROIs from 20 to 1000 ROIs. (bottom) FC matrices of DistKm ROIs from 20 to 1000 ROIs. **b,** From left to right, FC-SC correlation, FC-SC detection and FC-SC detection & correlation score, respectively. The solid line shows the FC vs. SC matrix (neuron), and the dashed line shows FC vs. SC matrix (synapse) at each ROI count. The vertical axis shows the correlation coefficient, averaged AUC and FC-SC detection & correlation score, respectively. The horizontal axis shows spatial smoothing size (voxels). **c,** Comparison between raw & smoothing (0 to 30 voxels) vs. Poly-tCompCor & smoothing (0 to 30 voxels) at each ROI count. Non-parametric Mann-Whitney U test was performed and Bonferroni correction was applied to correct for the familywise error rate (*** p<1.67e-4). **d,** Relation between FC-SC correlation and ROI count. (left vertical axis) Solid line shows FC-SC correlation (neuron) of SCKm and DistKm ROI type at each ROI count. (right vertical axis) The dashed line shows FC-SC detection (neuron) of SCKm and DistKm at each ROI count. **e,** Swarm plot of ROI volume of SCKm and DistKm at each ROI count.

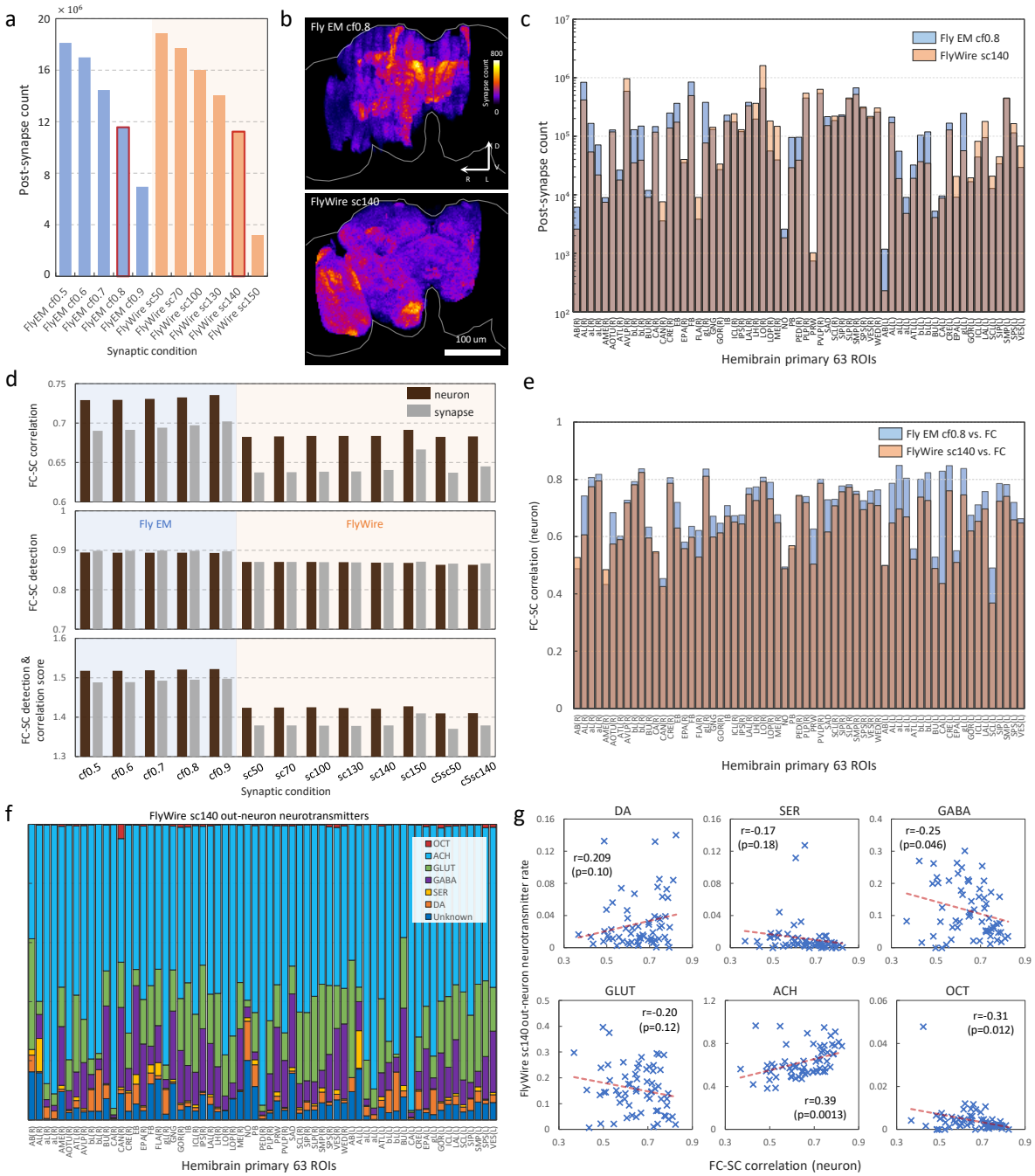

Fig. 3 Comparison between FlyEM and FlyWire connectome data. a, Bar graph of post-synapse count in hemibrain region from FlyEM and FlyWire connectome data. The vertical axis shows post-synapse count, and the horizontal axis shows confidence thresholds for FlyEM and Cleft score thresholds for FlyWire. **b,** (top) Maximum Z-projection of synapse point cloud of FlyEM (confidence thresholds=0.8 [hereafter, cf0.8]) (bottom) Maximum Z-projection of synapse point cloud of FlyWire (Cleft score threshold=140 [hereafter, sc140]) **c,** Bar graph of post-synapse count in hemibrain primary ROIs. Blue bar shows FlyEM (cf0.8), red bar shows FlyWire (sc140). The vertical axis shows post-synapse count, and the horizontal axis shows hemibrain primary ROIs. **d,** Bar graphs of FC-SC correlation, FC-SC detection, and FC-SC detection & correlation score, respectively. The horizontal axis shows confidence thresholds for FlyEM and Cleft score thresholds for FlyWire. **e,** Bar graph of FC-SC correlation in hemibrain primary ROIs. Blue bars show FlyEM (cf0.8) vs FC (neuron), red bars show FlyWire (sc140) vs FC (neuron). The vertical axis shows FC-SC correlation, and the horizontal axis shows hemibrain primary ROIs. **f,** Bar graph of neurotransmitter rate of output neurons in hemibrain primary ROIs based on FlyWire (sc140) connectome data **[45]**. The horizontal axis shows hemibrain primary ROIs. (DA: dopamine, SER: serotonin, GABA, GLUT: glutamine, ACH: acetylcholine, OCT: octopamine) **g,** Scatter plots of neurotransmitter rate of output neurons vs. FC-SC correlation (neuron) in hemibrain primary ROIs (FlyWire sc140). Each of the six neurotransmitters was compared.

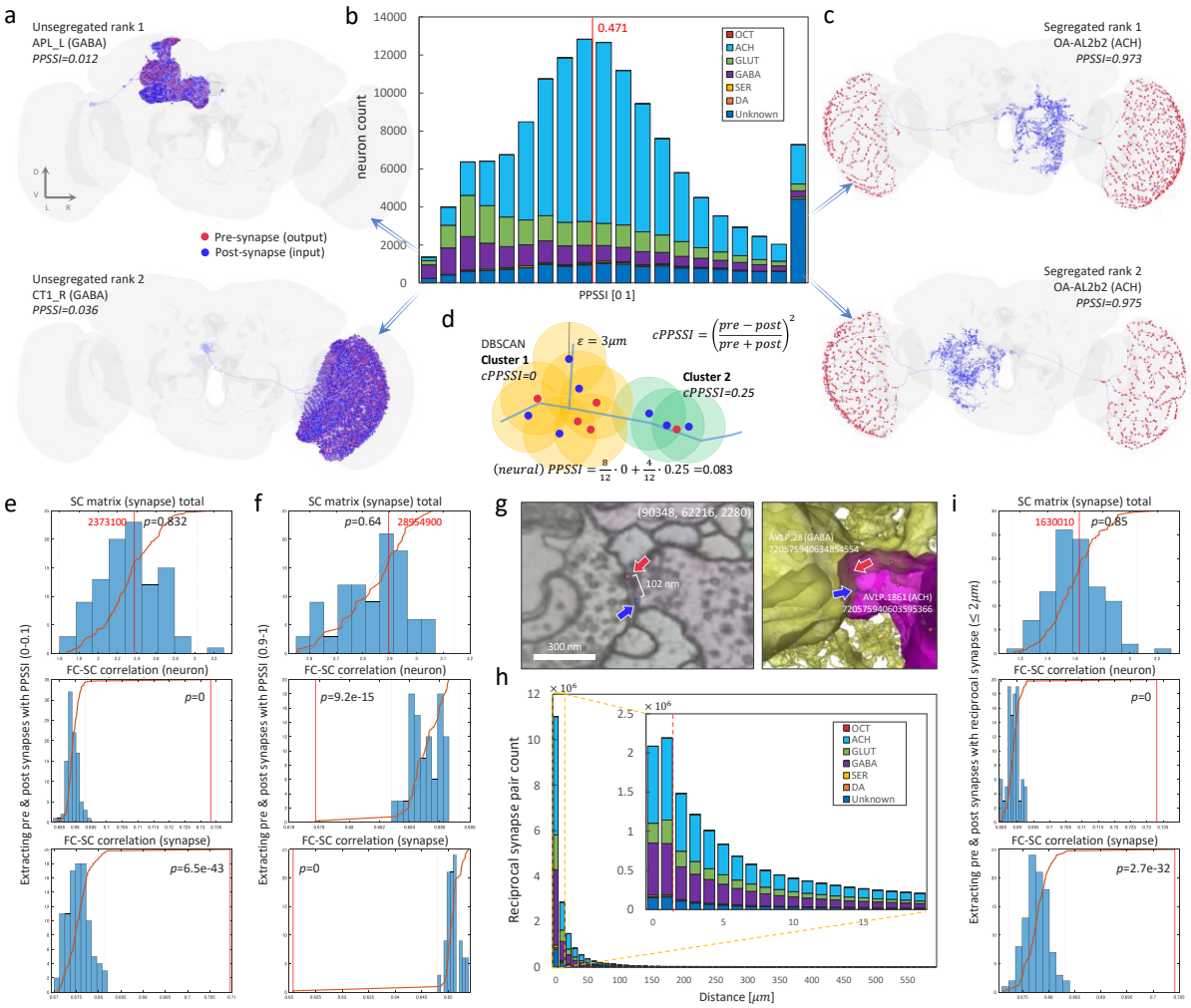

Fig. 4 Quantification of pre- and post-synapse segregation, and the relationship between FC and synapses. a, Unsegregated first (APL_L cell) and second (CT1_R cell) ranking in FlyWire (sc140) connectome data. A red dot shows pre-synapse, a blue dot shows post-synapse. **b,** The PPSSI histogram of all neurons (139,255) in FlyWire (sc140) connectome data. The vertical axis shows neuron count, and the horizontal axis shows PPSSI [0 1]. **c,** Segregated first (OA-AL2b2 cell) and second (OA-AL2b2 cell) ranking in FlyWire (sc140) connectome data. **d,** Schematic image of pre- and post-synapse clustering based on DBSCAN, and calculation of cPPSSI and PPSSI. **e,** Histogram of null SC matrices (blue bar) and extracted SC matrix with PPSSI (0-0.1) (red solid line). Black dotted line shows cumulative distribution function of the normal distribution, brown solid line shows cumulative distribution function of null & extracted SC matrices, and red dotted line shows Bonferroni-corrected p<0.05 threshold. Top shows SC matrix (synapse) total, middle shows FC-SC correlation (neuron), and bottom shows FC-SC correlation (synapse). **f,** Histogram of null SC matrices and extracted SC matrix with PPSSI (0.9-1). **g,** Example of a reciprocal-synapse in the EM image (left) and in 3D (right). **h,** Histogram of reciprocal-synaptic minimum distances in FlyWire (sc140) connectome data. The vertical axis shows reciprocal-synapse pair count, and the horizontal axis shows distance [μm]. **i,** Histogram of null SC matrices and extracted SC matrix for reciprocal-synapses ($\leq 2\mu m$).

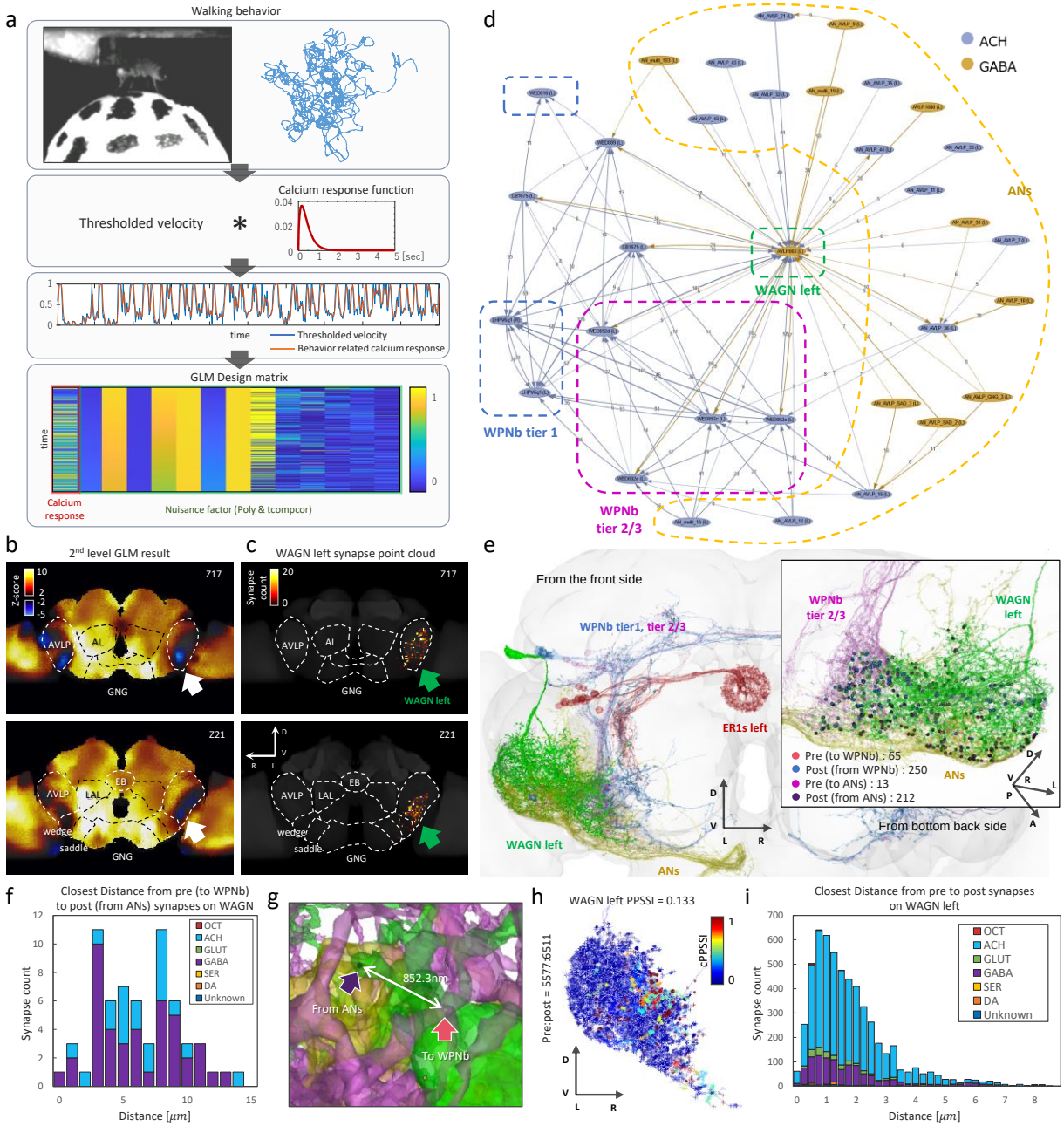

Fig. 5 General Linear Model analysis result and Wedge-AVLP GABA neuron. a, Schematic image of GLM analysis. From the top, experimental image and walking trajectory, calcium response function, thresholded velocity, and GLM design matrix, respectively. **b,** 2nd level (group) GLM analysis result from 9 flies. Top shows Z=17 slice of the resized FDA template, and the bottom shows the Z=21 slice. The white arrow indicates the suppressed region during the fly walking task. **c,** Synapse point cloud of the left WAGN in FlyWire (sc140) connectome data. Top shows Z=17 slice of the resized FDA template, and bottom shows the Z=21 slice. **d,** Network graph of the left WAGN, ANs, WPNb tier 1 and tier 2/3 neurons from FlyWire codex (sc50, connection threshold>5). Blue is acetylcholine, ocher is GABA neuron. The small number on the edges shows synapse count. **e,** 3D image of the left WAGN, ANs, WPNb tier 1, tier 2/3 and left ER1 neurons, frontal view. Inside the black square shows the left WAGN, ANs and WPNb tier 2/3 from the back side. **f,** Histogram of closest distance from pre-synapse (to WPNb) to post-synapse (from ANs) in the left WAGN. Horizontal axis shows distance [μm]. Neurotransmitter indicates input ANs to post-synapses. **g,** Example 3D image of pre-synapse (to WPNb) to post-synapse (from ANs). **h,** All pre- and post-synapses of the left WAGN from the front. Color indicates cPPSSI in each synapse. **i,** Histogram of closest distance from pre-synapse to post-synapse in the left WAGN. The horizontal axis shows distance [μm]. Neurotransmitter indicates input neurons to post-synapses.

Data Availability

Whole-brain calcium imaging data and walking behavior data in *Drosophila Melanogaster* can be downloaded from DANDI web site (https://dandiarchive.org/dandiset/000727/0.240106.0043). FlyWire connectome data can be downloaded from flywire codex (https://codex.flywire.ai/) and Zenodo web site (https://zenodo.org/records/10676866). FlyEM connectome data can be downloaded from Janeria's DVID web site (https://dvid.io/blog/release-v1.2/).

Code Availability

Software and code used in the current study is open source and publicly available from https://github.com/takuto-okuno-riken/flywalk

Authors' Contributions

T.O. conceived of the presented idea. T.O. developed the theory, performed the computations. T.O. downloaded and processed fly data. T.O., A.W., H.O. and J.H. discussed the results and contributed to the final manuscript.

Ethics declarations

All experimental procedures were approved by the Experimental Animal Committee of RIKEN or by the Experimental Animal Committee of the National Center of Neurology and Psychiatry. The marmosets were handled by the "Guiding Principles of the Care and Use of Animals in the Field of Physiological Science" formulated by the Japanese Physiological Society.

Competing interests

The authors declare that they have no competing interests.

Extended Data Figures

Extended Data Fig.1-1 Schematic image of registration process and connectome data transformation in *Drosophila melanogaster*. a, Schematic image of calcium image registration to the resized FDA template. Motion and slice timing correction were conducted using SPM12 [57], and the averaged NIfTI image was registered by ANTs [58] to the resized FDA template. Lastly, 4D NIfTI images were transformed using the transformation information. **b,** Schematic image of synapse points transformation from FlyWire space to the resized FDA template. **c,** Schematic image of synapse points transformation from FlyEM space to resized FDA template.

<u>Extended Data Fig.1-2</u> Pre- and Post-synapses of pyramidal cell in human temporal cortex layer 3-4. a, (left) Input to (post-synapses) a pyramidal cell in the human temporal cortex, from EM connectome data [39]. (center insert) A slice of human temporal cortex and target pyramidal cell. (right) Output from (pre-synapses) a pyramidal cell in the human temporal cortex, from EM connectome data. Blue dots show post-synaptic sites, Red dots show pre-synaptic sites.

<u>Extended Data Fig.2-1</u> Investigating spatial smoothing size, and high-pass filtering. a, (top) Example z-slice of reduced FDA template with SCKm ROIs from 20 to 1000 ROIs. (middle) SC matrices (neuron) of SCKm ROIs from 20 to 1000 ROIs. (bottom) FC matrices of SCKm ROIs from 20 to 1000 ROIs. **b,** From left to right, FC-SC correlation, FC-SC detection, and FC-SC detection & correlation score, respectively. Solid lines shows FC vs. SC matrix (neuron), and dashed lines shows FC vs. SC matrix (synapse) for each ROI count. The vertical axis shows the correlation coefficient, averaged AUC, and FC-SC detection & correlation score, respectively. The horizontal axis shows spatial smoothing size (voxels). **c,** Scatter plot of FC-SC correlation in the marmoset left cortex [10] (145 injection × 9862 voxels, r=0.379). **d,** Result of high-pass filtering and nuisance factor removal combination of DistKm ROIs. From left to right, FC-SC correlation, FC-SC detection, and FC-SC detection & correlation score, respectively. The high-pass filter degraded the FC-SC relationship.

<u>Extended Data Fig.3-1</u> Comparison between FlyEM and FlyWire connectome data. a, (left) A scatter plot of regional post-synapse count between FlyEM (cf0.8) and FlyWire (sc140) in the hemibrain primary 63 ROIs. The Pearson correlation is not so similar, r=0.778, but the Spearman correlation is much more similar, r=0.9. (right) A scatter plot of log10 of the regional post-synapse count between FlyEM (cf0.8) and FlyWire (sc140) in the hemibrain primary ROIs. Pearson correlation shows r=0.919, a higher similarity. **b,** From left to right, FC-SC correlation, FC-SC detection, and FC-SC detection & correlation score, respectively. Solid lines shows FC vs. SC matrix (neuron), and dashed lines shows FC vs. SC matrix (synapse) of FlyEM (cf0.5-0.9) and FlyWire (sc50-140) corresponding Fig.3d. The vertical axis shows the correlation coefficient, averaged AUC, and FC-SC detection & correlation score, respectively. The horizontal axis shows spatial smoothing & nuisance factor removal combinations. **c,** From left to right, SC matrix (neuron) (FlyEM cf0.8), SC matrix (neuron) (FlyWire sc140) and FC matrix (Poly-tCompCor, no smoothing) in the hemibrain primary 63 ROIs. **d,** (right) SC matrix (neuron) result of FlyEM (cf0.8) minus FlyWire (sc140) in hemibrain primary ROIs. (left) SC matrix (synapse) result of FlyEM (cf0.8) minus FlyWire (sc140). FlyEM shows a higher number of synaptic connections.

<u>Extended Data Fig.3-2</u> In-neuron neurotransmitters and comparison between FlyEM and FlyWire connectome data. a, Bar graph of neurotransmitter rate of input neurons in hemibrain primary 63 ROIs based on FlyWire (sc140) connectome data [44]. The horizontal axis shows hemibrain primary ROIs. (DA: dopamine, SER: serotonin, GABA, GLUT: glutamine, ACH: acetylcholine, OCT: octopamine) **b,** Scatter plots of neurotransmitter rate of input neurons vs. FC-SC correlation (neuron) in hemibrain primary ROIs (FlyWire sc140). Each of the six neurotransmitters was compared. **c,** Comparison between FlyEM and FlyWire APL right neuron (synapse point cloud mask). Red voxels are FlyEM, green voxels are FlyWire, and yellow voxels are both. Sørensen-Dice index (0.716) shows similarity, so neuropil shape is similar between two. **d,** (left) A scatter plot of post-synapse count between FlyEM and FlyWire APL right neuron. Pearson correlation shows r=0.104, so not similar at all. (center) Same as left, but synapse point cloud was spatially smoothed by gaussian kernel (2 voxels). Similarity was increased (r=0.379). (right) Same as center, but smoothed by gaussian kernel (8 voxels). Similarity was increased (r=0.66). These results support that spatial smoothing can absorb inter-individual variability.

<u>Extended Data Fig.4-1</u> Quantification of pre- and post-synapse segregation and relationship between FC and synapses (FlyEM). a, Unsegregated first (APL_L cell) and second (DPM_R cell) ranked cells in the FlyEM (cf0.8) connectome data. Red dots shows pre-synapses, blue dot shows post-synapses. **b,** The PPSSI histogram of hemibrain neurons (99,644) in FlyEM (cf0.8) connectome data. The vertical axis shows neuron count, and the horizontal axis shows PPSSI [0 1]. **c,** Segregated first (AOTU019_R cell) and second (DNa02_R cell) ranked cells in the FlyEM (cf0.8) connectome data. **d,** Histogram of null SC matrices (blue bar) and extracted SC matrix with PPSSI (0-0.1) (red solid line). The black dotted line shows the cumulative distribution function of the normal distribution, the brown solid line shows the cumulative distribution function of null & extracted SC matrices, and the red dotted line shows the Bonferroni-corrected $p<0.05$ threshold. Top shows the SC matrix (synapse) total, middle shows FC-SC correlation (neuron), and bottom shows FC-SC correlation (synapse). **e,** Histogram of null SC matrices and extracted SC matrix with PPSSI (0.9-1). **f,** Example of a reciprocal-synapse in the EM image (left) and 3D image (right). g, Histogram of reciprocal-synaptic minimum distances in the FlyEM (cf0.8) connectome data. The vertical axis shows reciprocal-synapse pair count, and the horizontal axis shows distance [μm]. **h,** Histogram of null SC matrices and extracted SC matrix with reciprocal-synapses (≤2μm). **i,** The segregation index histogram of all neurons (139,255) in FlyWire (sc140) connectome data. The horizontal axis shows segregation index [0 1]. **j,** The segregation index histogram of hemibrain neurons (99,644) in the FlyEM (cf0.8) connectome data. The horizontal axis shows the segregation index [0 1].

<u>Extended Data Fig.4-2</u> Reciprocal synapses of CT1 and APL neurons, and synapse point cloud for several conditions. a, Histogram of reciprocal-synaptic minimum distances of the CT1-R neuron in the FlyWire (sc140) connectome data. The vertical axis shows reciprocal-synapse pair count, and the horizontal axis shows distance [μm]. **b,** Skeleton view of the CT1-R neuron. Red dots are pre-synapses and blue dots are post-synapses of reciprocal synapses ($\leq 2\mu m$). **c,** Histogram of reciprocal-synaptic minimum distances of the APL-R neuron in the FlyWire (sc140) connectome data. **d,** Skeleton view of the APL-R neuron, the same way as b. **e,** (top) Maximum Z-projection of pre & post synapse point cloud within PPSSI (0-0.1) in the FlyEM data (cf0.8). (bottom) Maximum Z-projection of pre & post synapse point cloud within PPSSI (0-0.1) in the FlyWire data (sc140). **f,** The same as in e, but with the condition PPSSI in 0.9-1. **g,** The same as in e, but with the condition of only reciprocal synapses ($\leq 2\mu m$).

<u>Extended Data Fig.4-3</u> Unsegregated and segregated cell ranking examples (FlyWire sc140). a, Unsegregated cell ranking from 3rd to 11th in the FlyWire (sc140) connectome data. Red dots shows pre-synapses, blue dots shows post-synapses. **b,** Segregated cell ranking from 3rd to 11th.

<u>Extended Data Fig.4-4</u> Unsegregated and segregated cell ranking (FlyEM cf0.8). a, Unsegregated cell ranking from 3rd to 11th in the FlyEM (cf0.8) connectome data. Red dots shows pre-synapse, blue dots show post-synapses. **b,** Segregated cell ranking from 3rd to 11th.

<u>Extended Data Fig.5-1</u> Mechanosensory pathway from Wedge to Ellipsoid Body. a, 3D image of WL-L right, WED016 left, WPNb tier 1, and ER1 left neurons, frontal view. Black square insert shows WL-L right, WED016 left, WPNb tier 1 and ER1 left neurons from the left lateral view. **b,** Network graph of WL-L right, WED016 left, WPNb tier 1 and ER1 left neurons from the FlyWire codex (sc50, connection threshold≥5). Blue is for acetylcholine, ocher for GABA neurons. The small number on the edges shows synapse count.

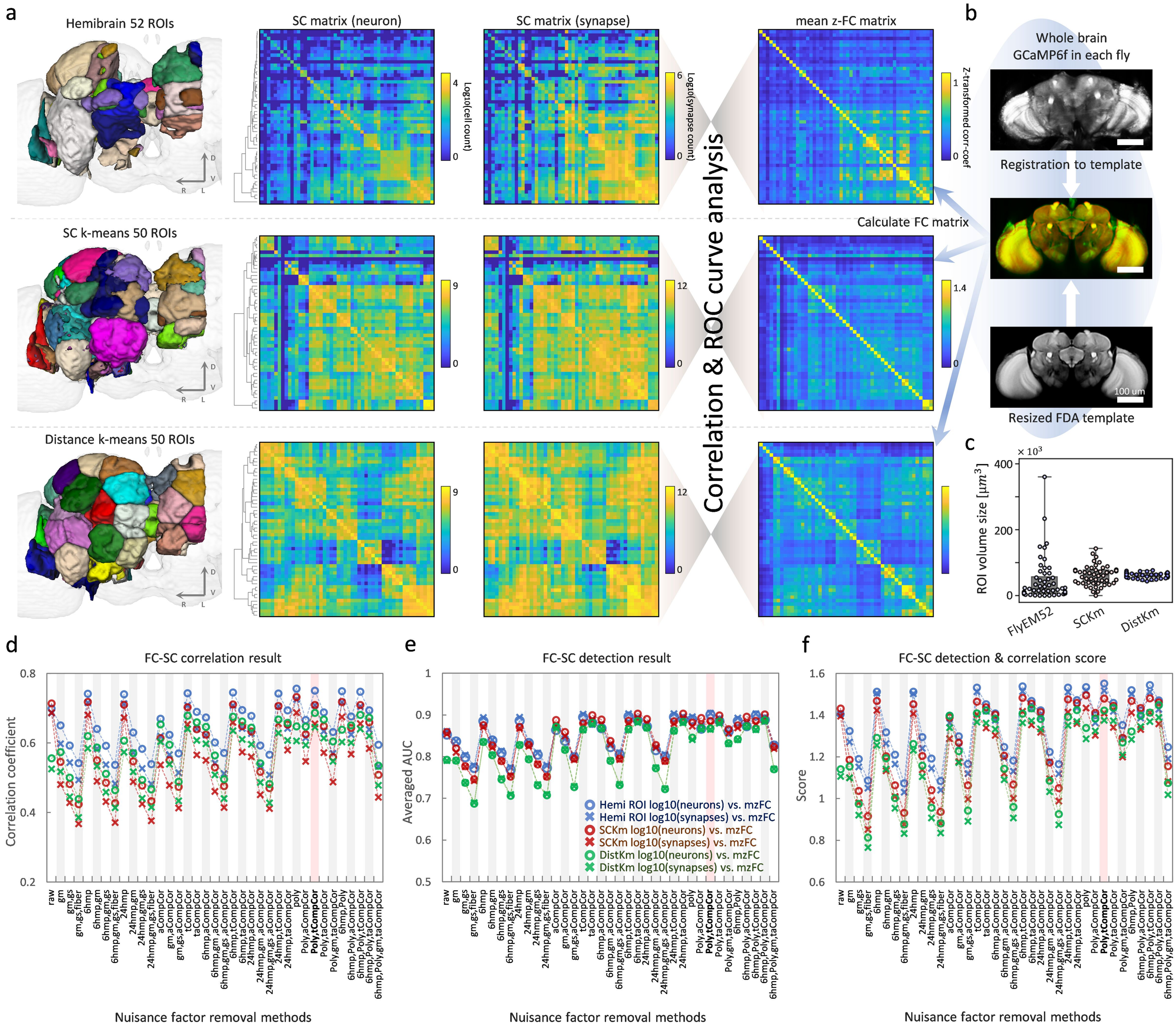
a
Hemibrain 52 ROIs
SC matrix (neuron)
SC matrix (synapse)
mean z-FC matrix
Log10(cell count)
Log10(synapse count)
Z-transformed corr-coef
SC k-means 50 ROIs
Distance k-means 50 ROIs
Correlation & ROC curve analysis
b
Whole brain GCaMP6f in each fly
Registration to template
Calculate FC matrix
Resized FDA template
100 um
c
ROI volume size [μm^3]
FlyEM52
SCKm
DistKm
d
FC-SC correlation result
Correlation coefficient
e
FC-SC detection result
Averaged AUC
Hemi ROI log10(neurons) vs. mzFC
Hemi ROI log10(synapses) vs. mzFC
SCKm log10(neurons) vs. mzFC
SCKm log10(synapses) vs. mzFC
DistKm log10(neurons) vs. mzFC
DistKm log10(synapses) vs. mzFC
f
FC-SC detection & correlation score
Score
Nuisance factor removal methods

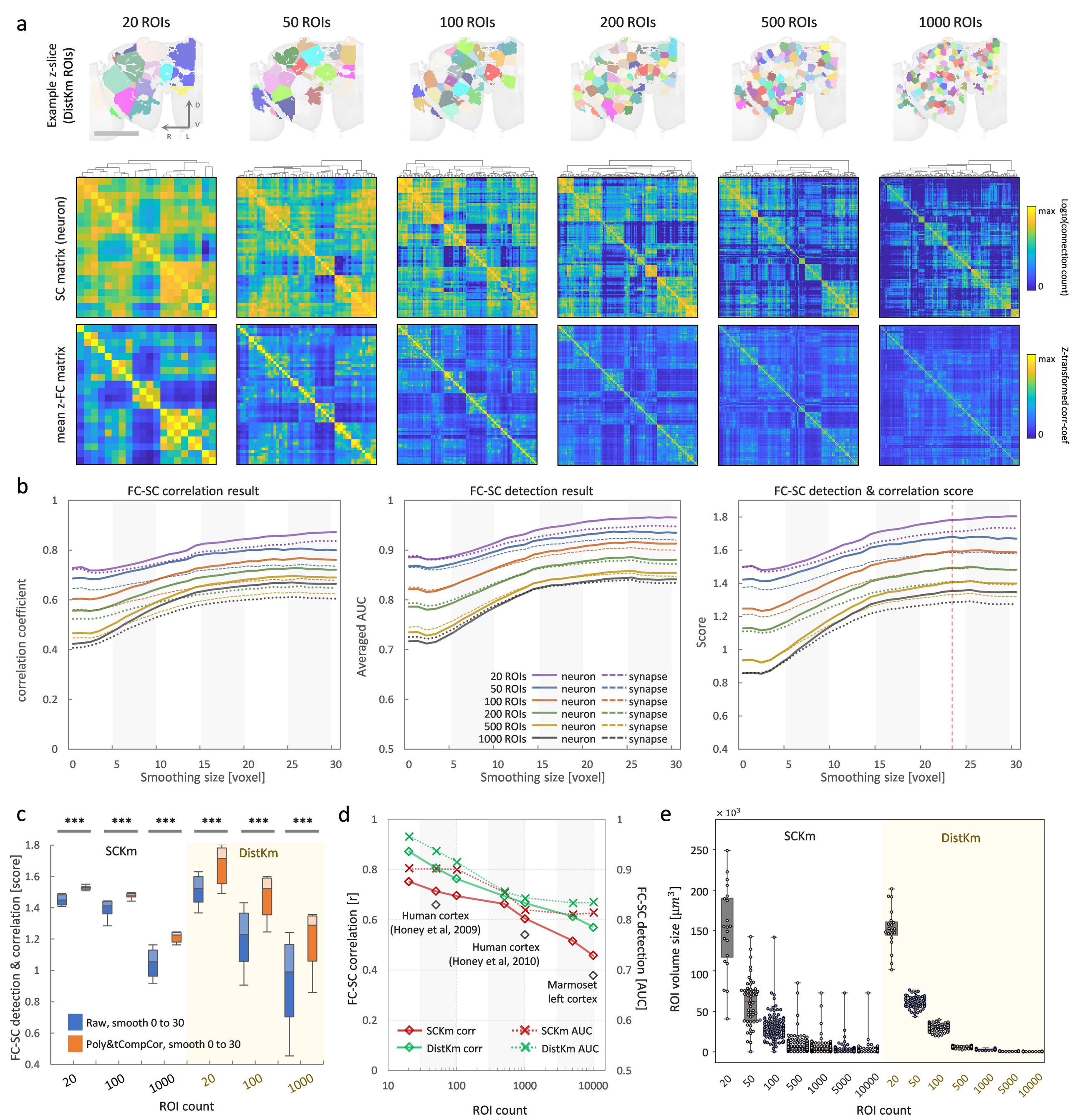
a
20 ROIs
50 ROIs
100 ROIs
200 ROIs
500 ROIs
1000 ROIs
Example z-slice (DistKm ROIs)
D
V
R
L
SC matrix (neuron)
mean z-FC matrix
max
0
Log10(connection count)
Z-transformed corr-coef
b
FC-SC correlation result
FC-SC detection result
FC-SC detection & correlation score
correlation coefficient
Averaged AUC
Score
Smoothing size [voxel]
20 ROIs neuron synapse
50 ROIs neuron synapse
100 ROIs neuron synapse
200 ROIs neuron synapse
500 ROIs neuron synapse
1000 ROIs neuron synapse
c
***
SCKm
DistKm
FC-SC detection & correlation [score]
Raw, smooth 0 to 30
Poly&tCompCor, smooth 0 to 30
ROI count
d
FC-SC correlation [r]
FC-SC detection [AUC]
Human cortex (Honey et al, 2009)
Human cortex (Honey et al, 2010)
Marmoset left cortex
SCKm corr
DistKm corr
SCKm AUC
DistKm AUC
ROI count
e
× 10³
ROI volume size [μm³]
SCKm
DistKm
ROI count

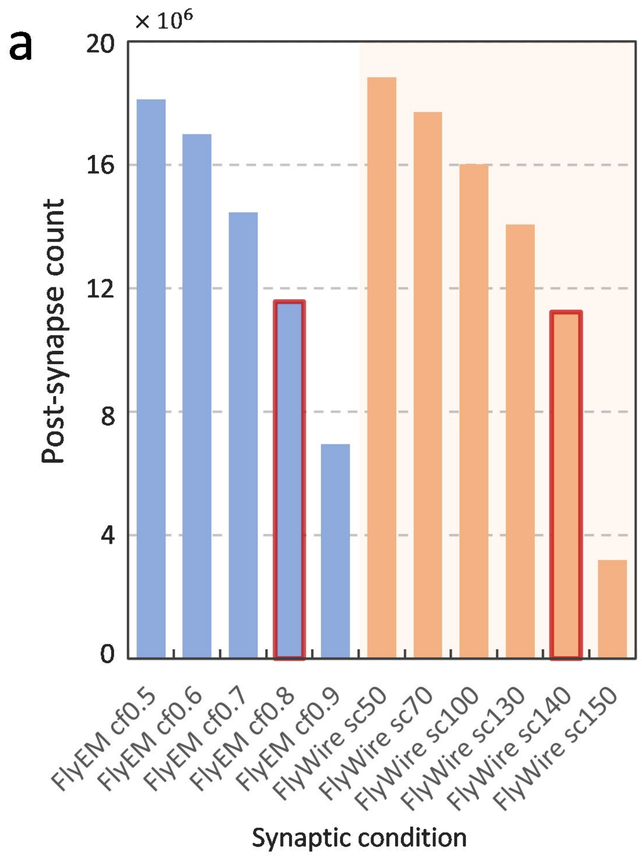
a
× 10^6
Post-synapse count
FlyEM cf0.5
FlyEM cf0.6
FlyEM cf0.7
FlyEM cf0.8
FlyEM cf0.9
FlyWire sc50
FlyWire sc70
FlyWire sc100
FlyWire sc130
FlyWire sc140
FlyWire sc150
Synaptic condition

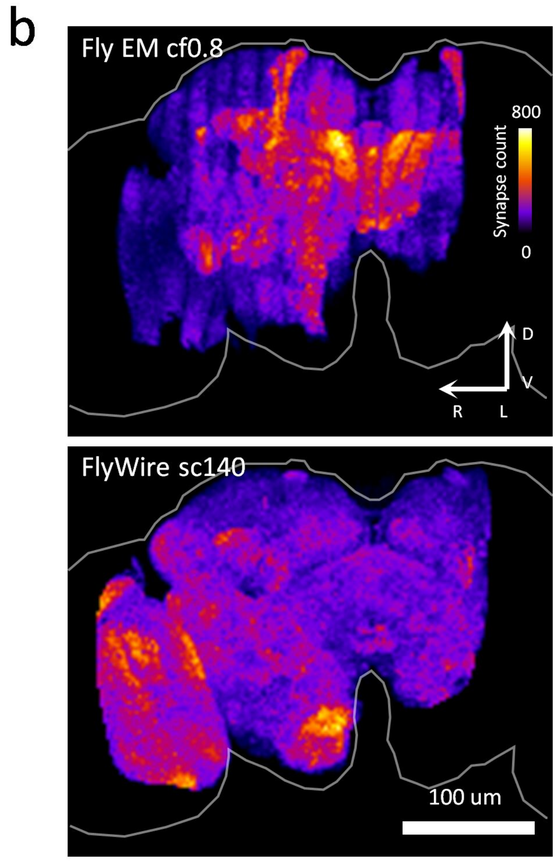
b
Fly EM cf0.8
Synapse count
800
0
D
V
R
L
FlyWire sc140
100 um

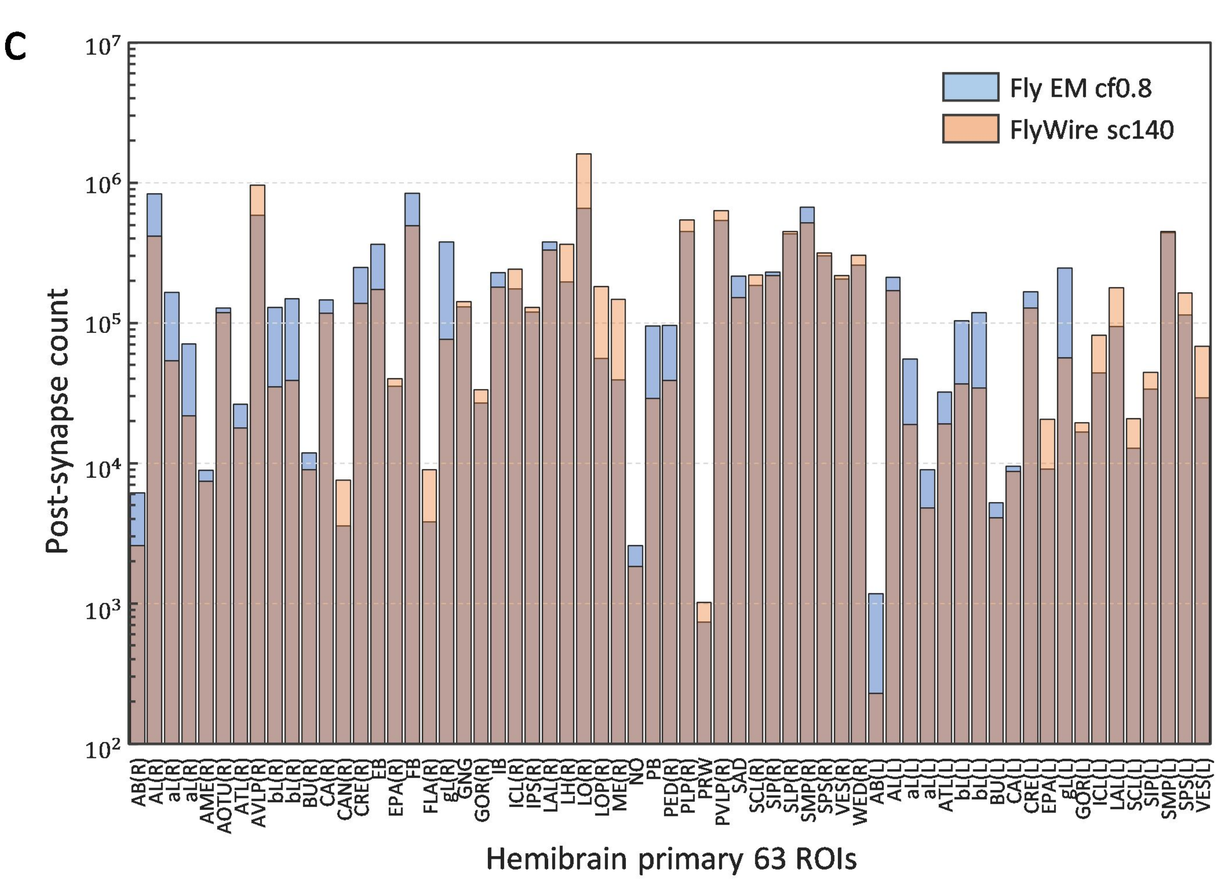
c
Fly EM cf0.8
FlyWire sc140
Post-synapse count
Hemibrain primary 63 ROIs

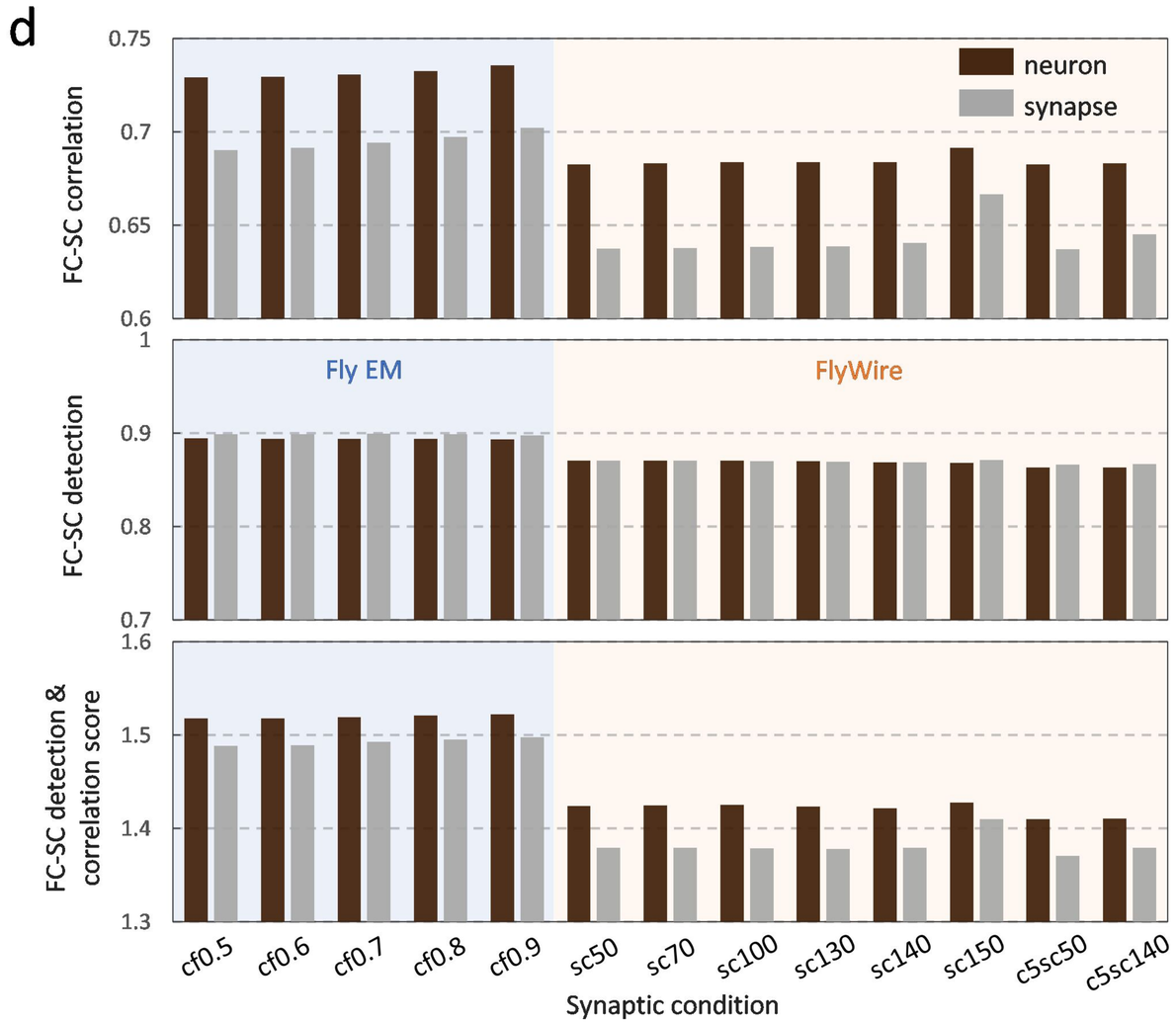
d
neuron
synapse
FC-SC correlation
Fly EM
FlyWire
FC-SC detection
FC-SC detection & correlation score
cf0.5
cf0.6
cf0.7
cf0.8
cf0.9
sc50
sc70
sc100
sc130
sc140
sc150
c5sc50
c5sc140
Synaptic condition

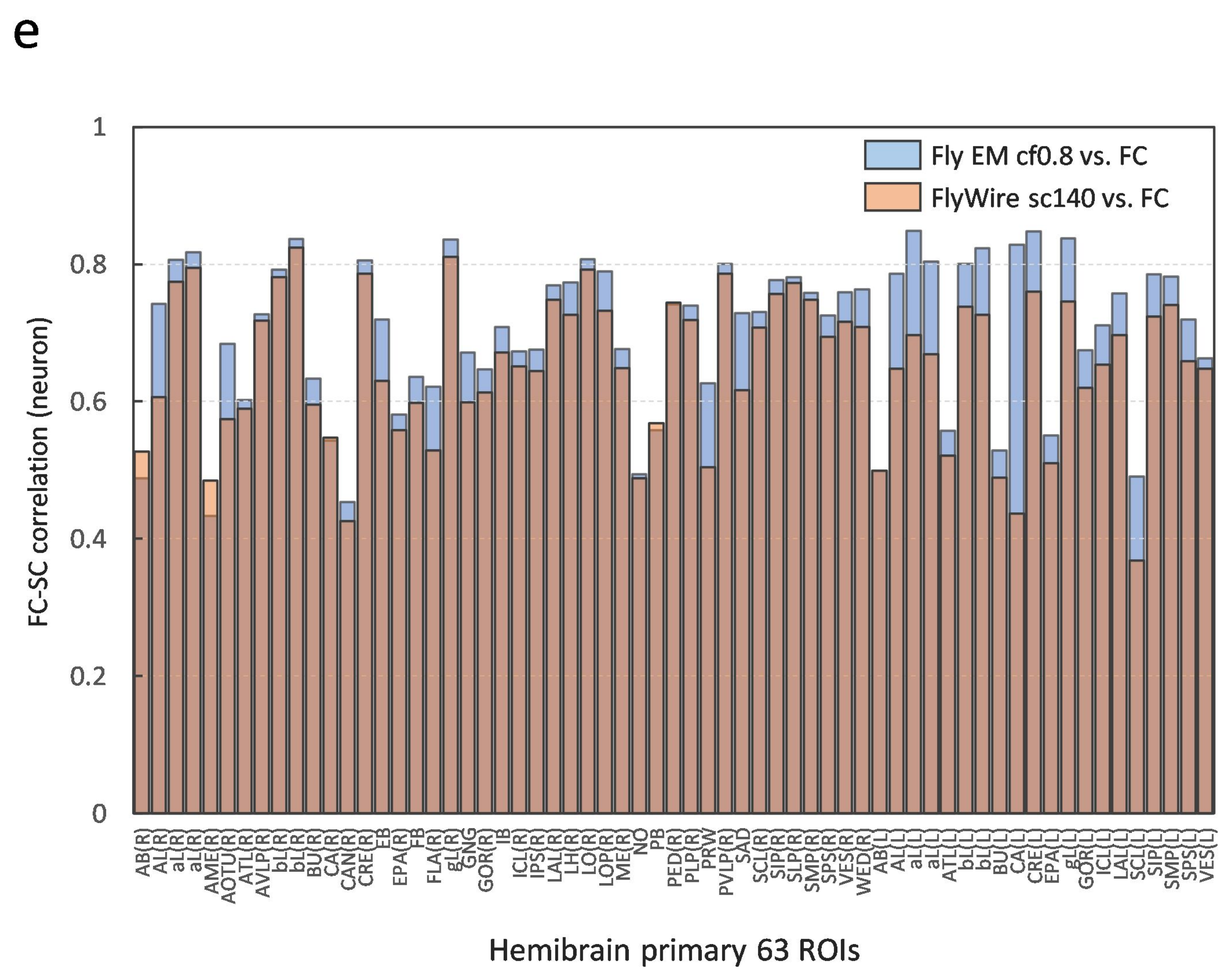
e
Fly EM cf0.8 vs. FC
FlyWire sc140 vs. FC
FC-SC correlation (neuron)
Hemibrain primary 63 ROIs

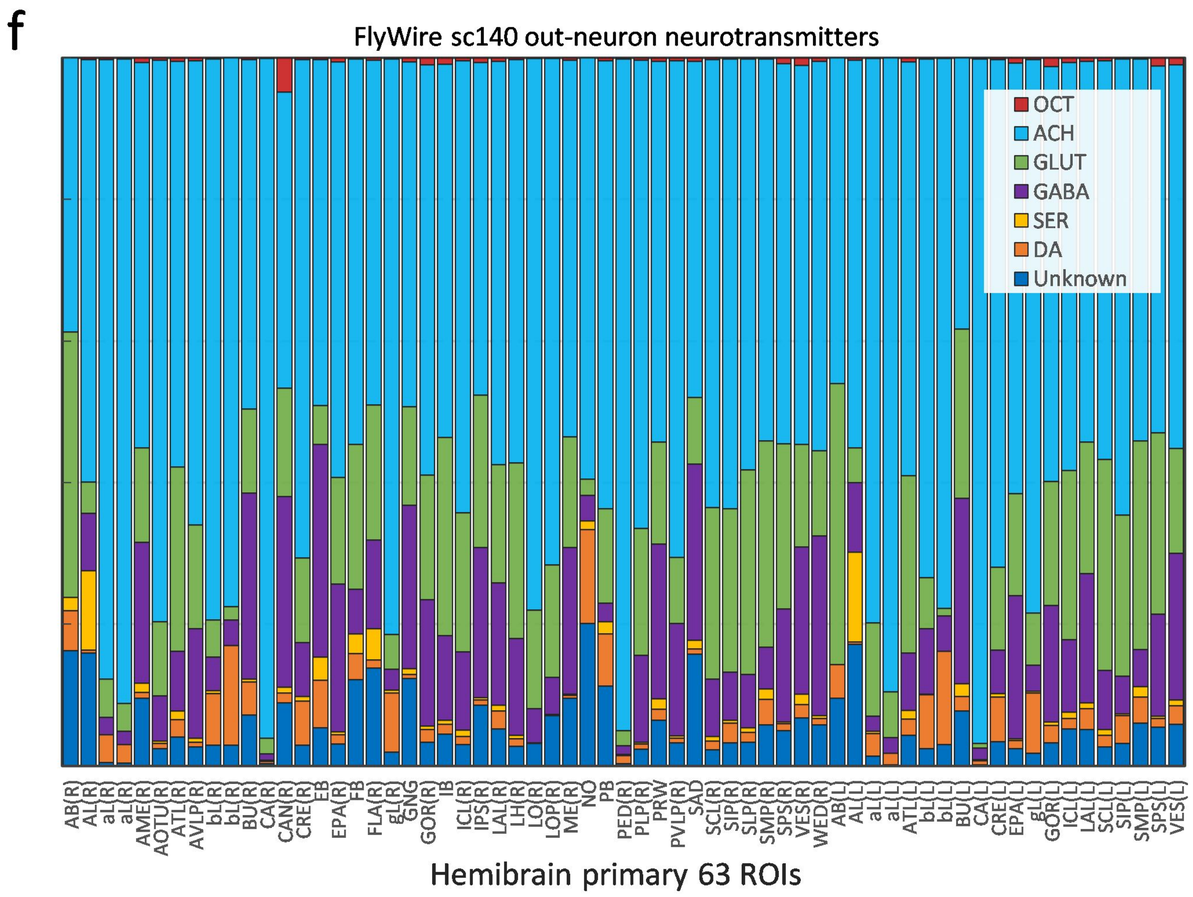
f
FlyWire sc140 out-neuron neurotransmitters
OCT
ACH
GLUT
GABA
SER
DA
Unknown
Hemibrain primary 63 ROIs

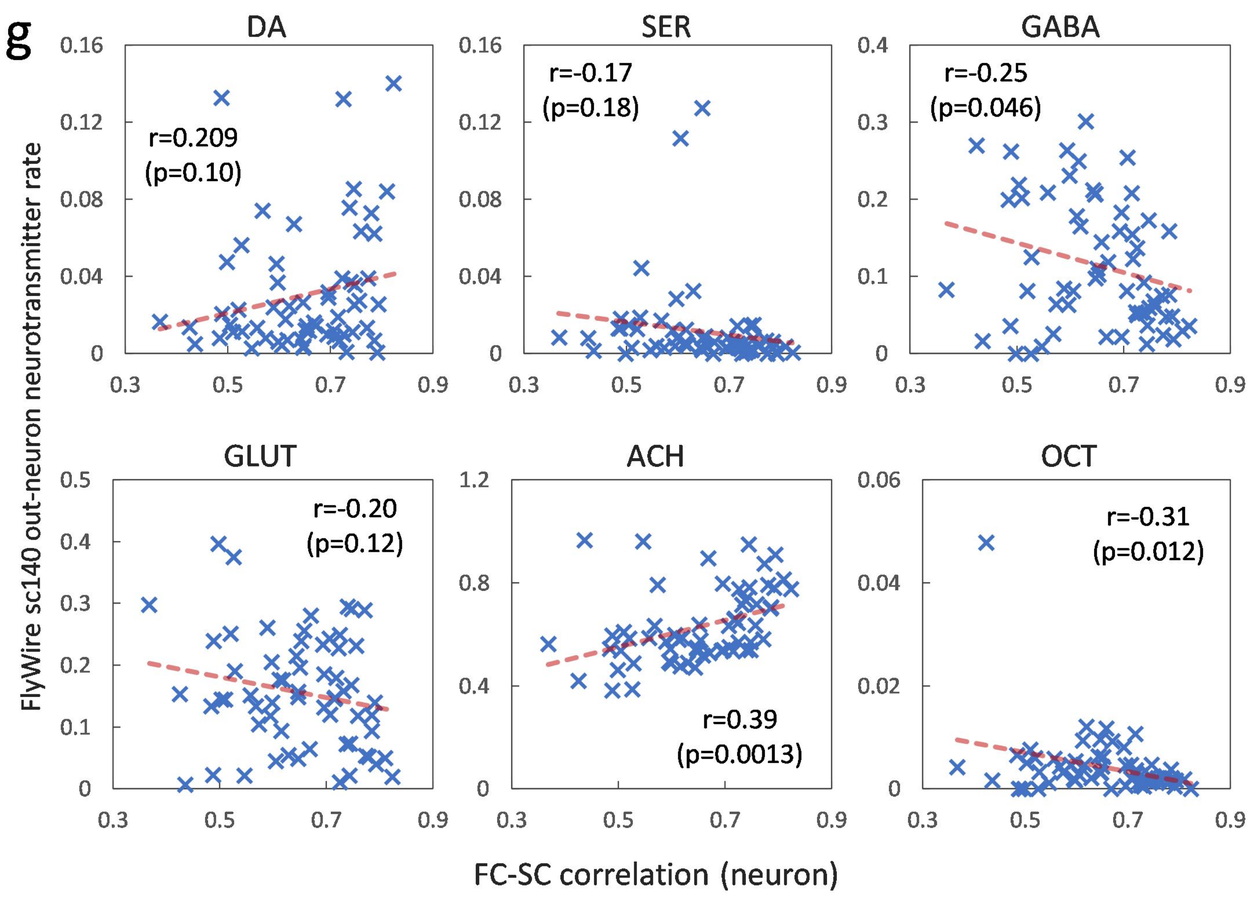
g
DA
r=0.209
(p=0.10)
SER
r=-0.17
(p=0.18)
GABA
r=-0.25
(p=0.046)
GLUT
r=-0.20
(p=0.12)
ACH
r=0.39
(p=0.0013)
OCT
r=-0.31
(p=0.012)
FlyWire sc140 out-neuron neurotransmitter rate
FC-SC correlation (neuron)

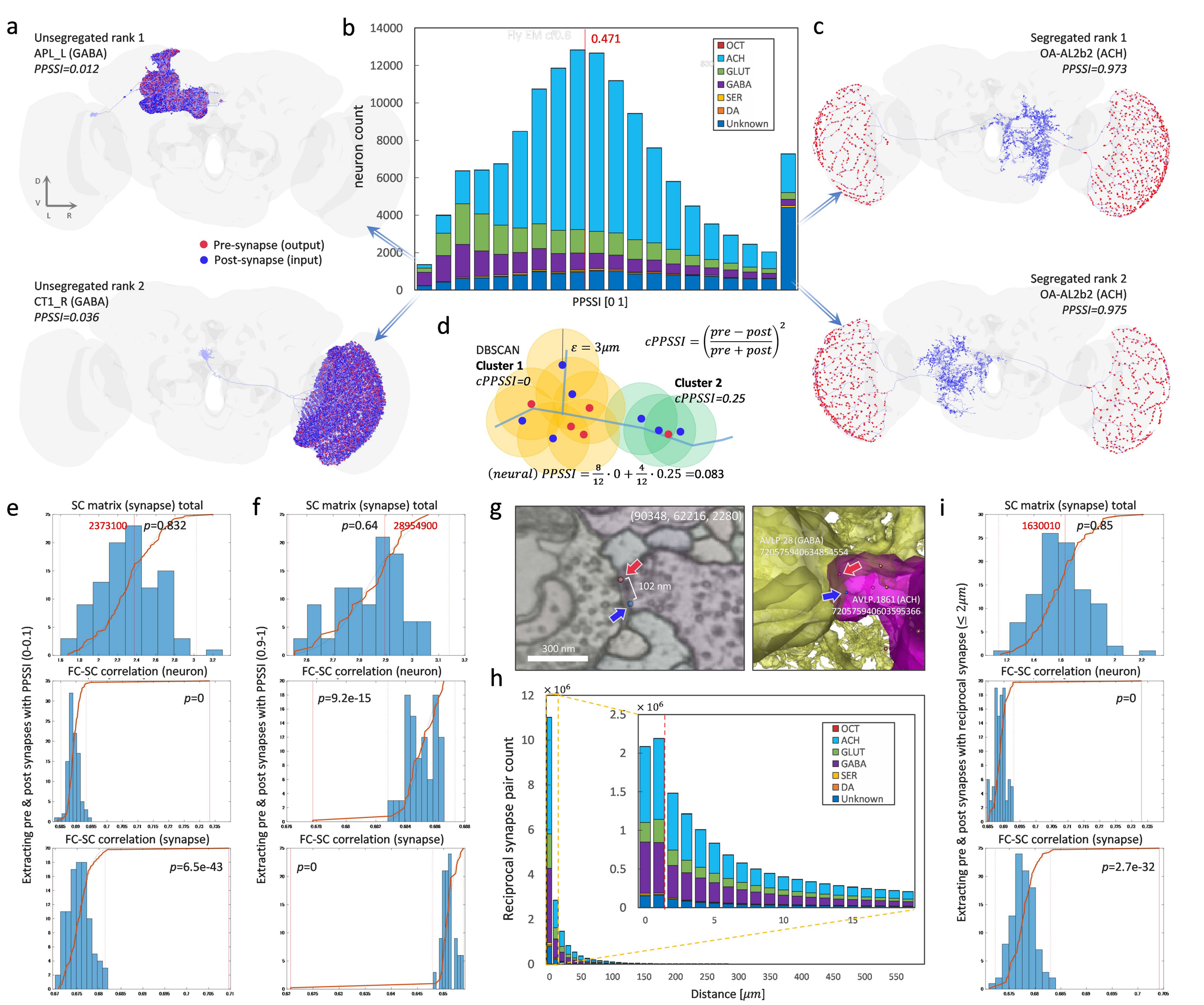
a
Unsegregated rank 1
APL_L (GABA)
PPSSI=0.012
D
V
L
R
Pre-synapse (output)
Post-synapse (input)
Unsegregated rank 2
CT1_R (GABA)
PPSSI=0.036
b
Fly EM cf0.8
0.471
neuron count
PPSSI [0 1]
OCT
ACH
GLUT
GABA
SER
DA
Unknown
c
Segregated rank 1
OA-AL2b2 (ACH)
PPSSI=0.973
Segregated rank 2
OA-AL2b2 (ACH)
PPSSI=0.975
d
DBSCAN
Cluster 1
cPPSSI=0
ε = 3μm
Cluster 2
cPPSSI=0.25
cPPSSI = (pre − post / pre + post)^2
(neural) PPSSI = 8/12 · 0 + 4/12 · 0.25 =0.083
e
SC matrix (synapse) total
2373100
p=0.832
FC-SC correlation (neuron)
p=0
FC-SC correlation (synapse)
p=6.5e-43
Extracting pre & post synapses with PPSSI (0-0.1)
f
SC matrix (synapse) total
p=0.64
28954900
FC-SC correlation (neuron)
p=9.2e-15
FC-SC correlation (synapse)
p=0
Extracting pre & post synapses with PPSSI (0.9-1)
g
(90348, 62216, 2280)
102 nm
300 nm
AVLP.28 (GABA)
720575940634854554
AVLP.1861 (ACH)
720575940603595366
h
Reciprocal synapse pair count
Distance [μm]
OCT
ACH
GLUT
GABA
SER
DA
Unknown
i
SC matrix (synapse) total
1630010
p=0.85
FC-SC correlation (neuron)
p=0
FC-SC correlation (synapse)
p=2.7e-32
Extracting pre & post synapses with reciprocal synapse (≤ 2μm)

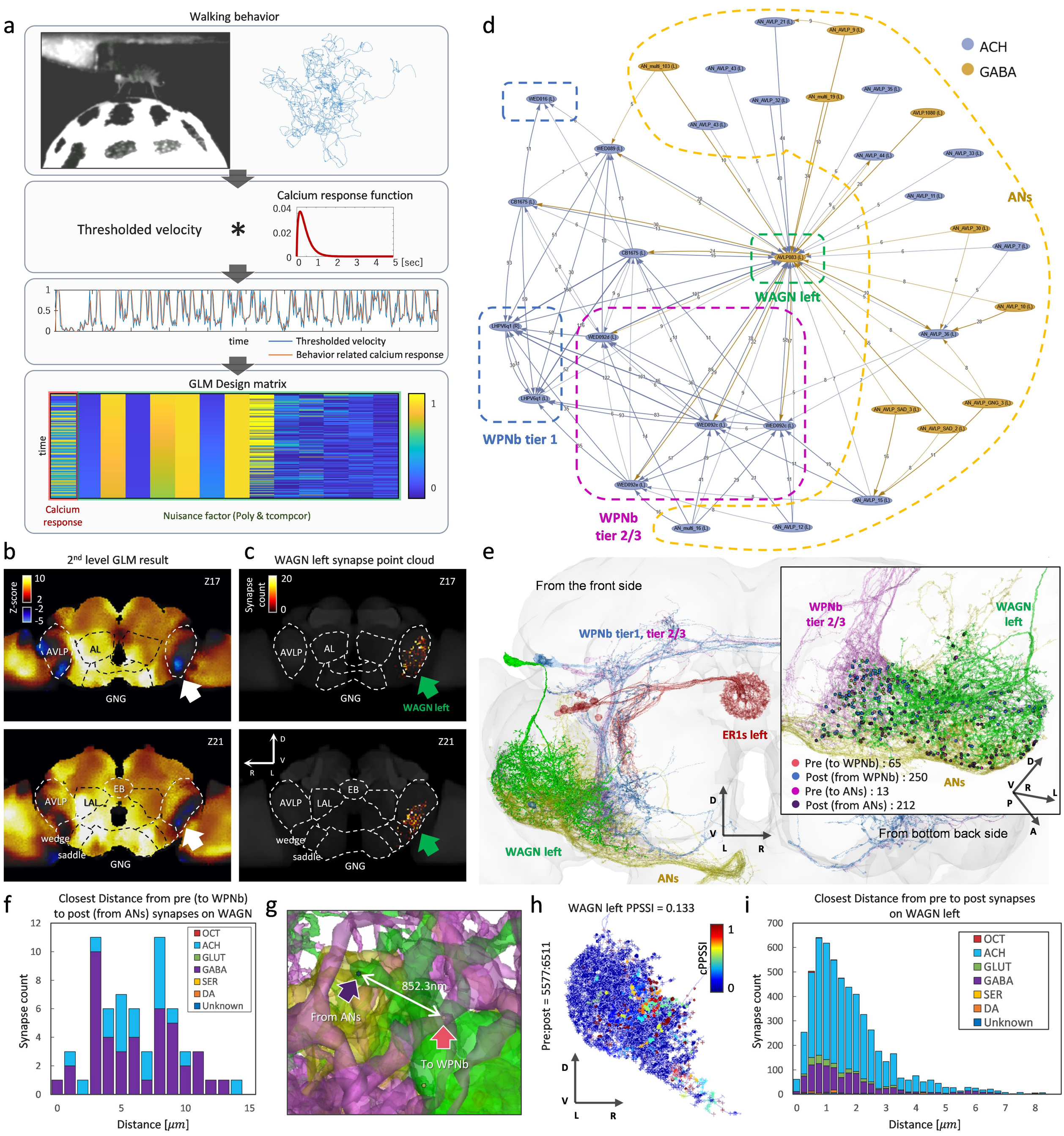
a
Walking behavior
Calcium response function
Thresholded velocity
time
Thresholded velocity
Behavior related calcium response
GLM Design matrix
time
Calcium response
Nuisance factor (Poly & tcompcor)
b
2nd level GLM result
Z-score
Z17
Z21
AVLP
AL
GNG
LAL
EB
wedge
saddle
c
WAGN left synapse point cloud
Synapse count
WAGN left
d
ACH
GABA
ANs
WAGN left
WPNb tier 1
WPNb tier 2/3
e
From the front side
WPNb tier1, tier 2/3
ER1s left
WAGN left
ANs
WPNb tier 2/3
WAGN left
Pre (to WPNb) : 65
Post (from WPNb) : 250
Pre (to ANs) : 13
Post (from ANs) : 212
From bottom back side
f
Closest Distance from pre (to WPNb) to post (from ANs) synapses on WAGN
Synapse count
Distance [μm]
OCT
ACH
GLUT
GABA
SER
DA
Unknown
g
852.3nm
From ANs
To WPNb
h
WAGN left PPSSI = 0.133
Pre:post = 5577:6511
cPPSSI
i
Closest Distance from pre to post synapses on WAGN left
Synapse count
Distance [μm]

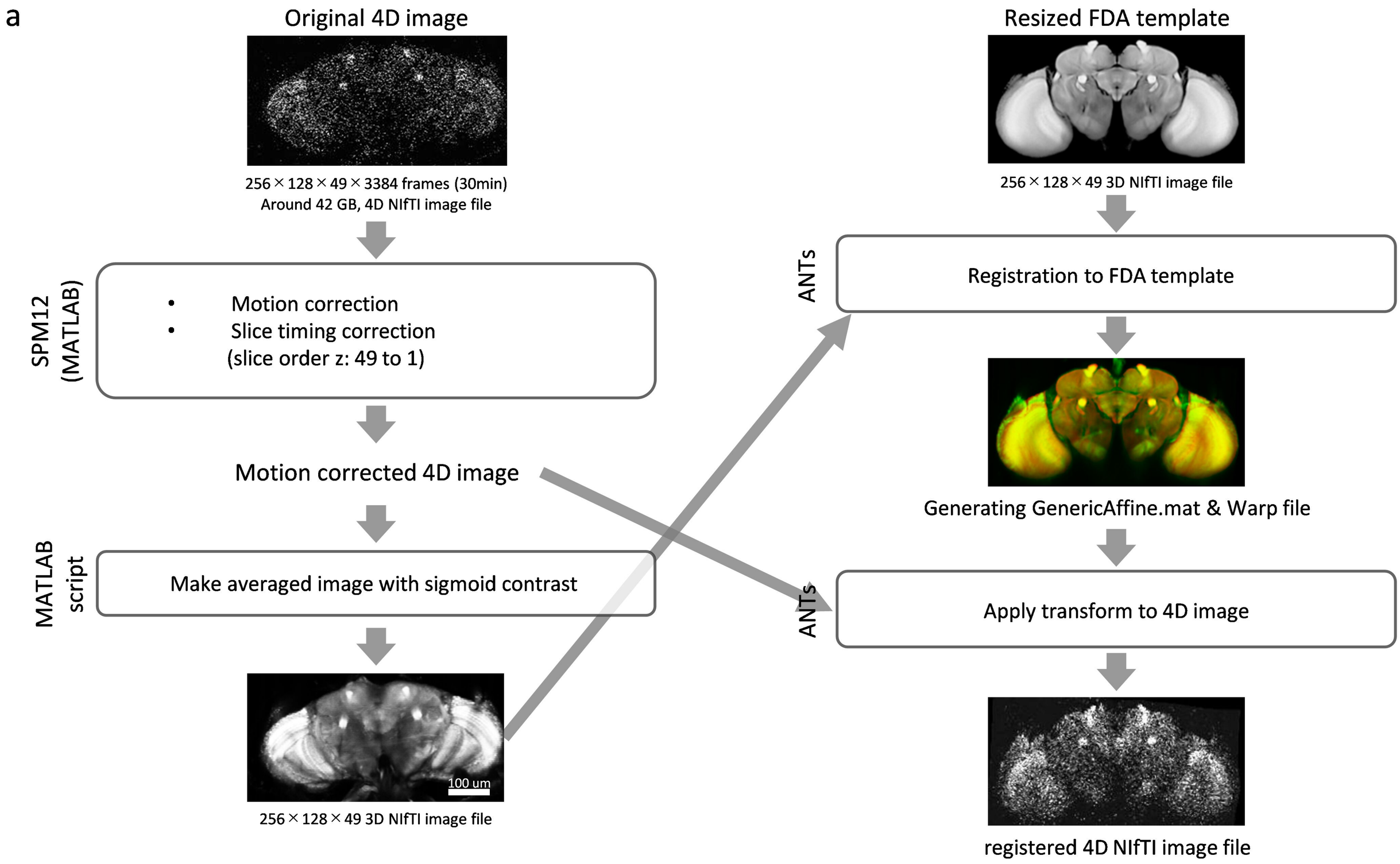

b

Transform synapse points from FlyWire space to JRC2018_FEMALE template by **Python** with **navis-flybrains**

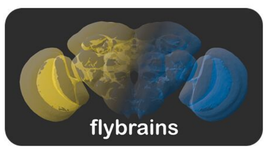

Flip left and right on template on JRC2018_FEMALE template

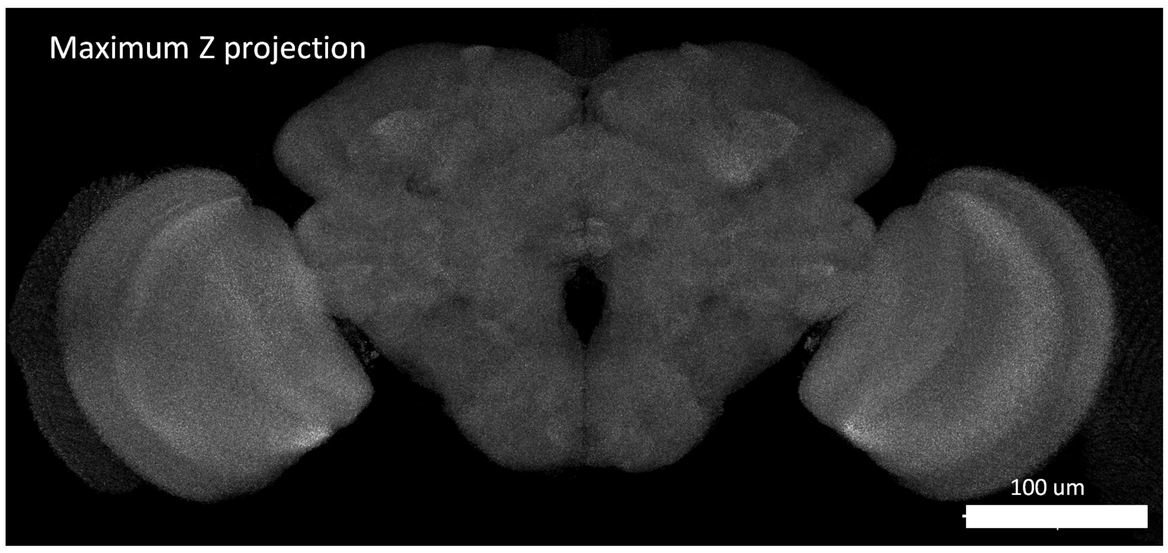

FlyWire synapse point cloud on JRC2018_FEMALE template

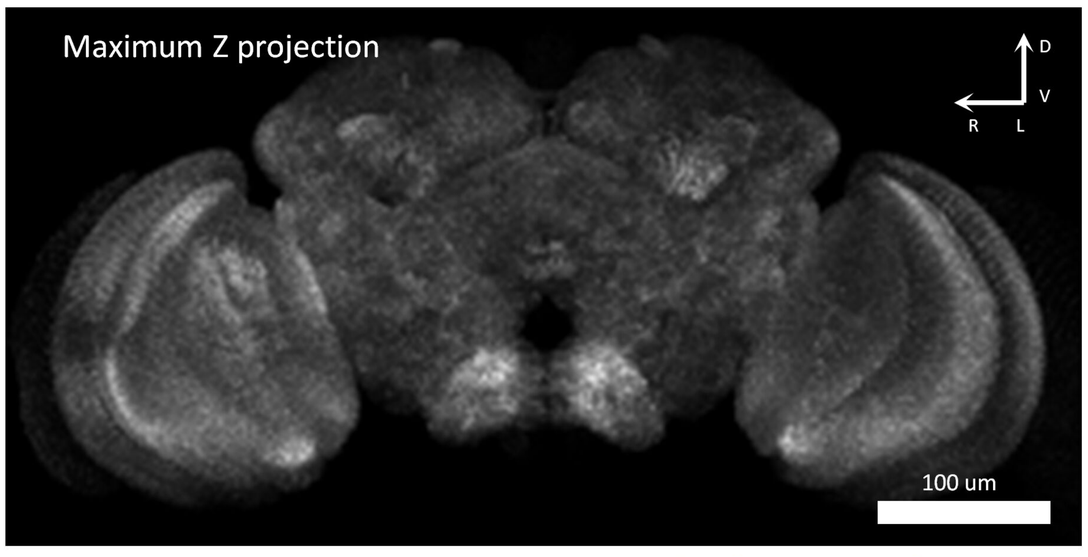

FlyWire synapse point cloud on resized FDA template

c

Transform synapse points from FlyEM space to JRC2018_FEMALE template by **Python** with **navis-flybrains**

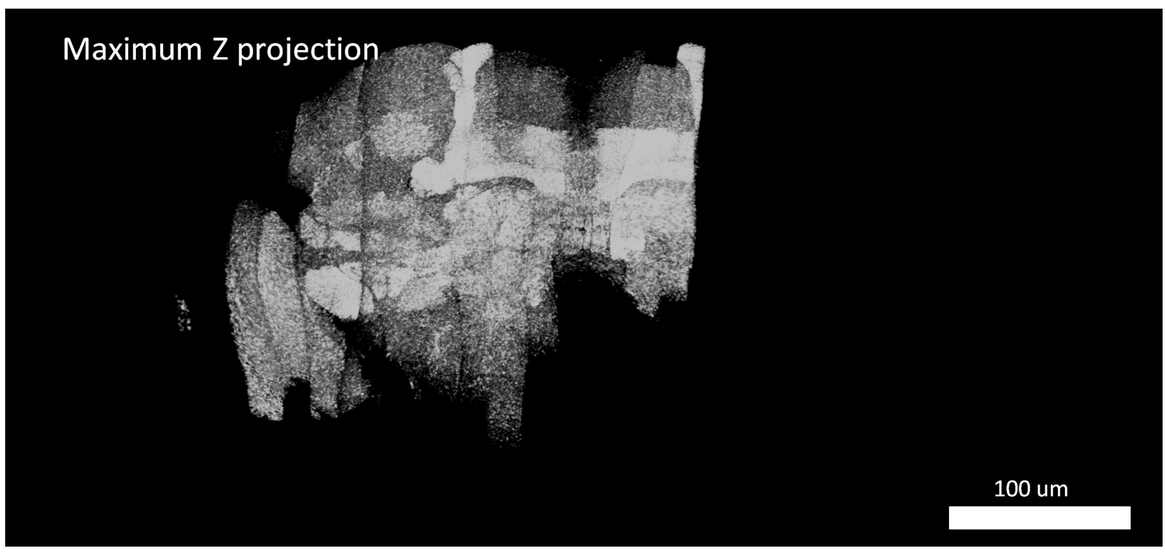

FlyEM synapse point cloud on JRC2018_FEMALE template

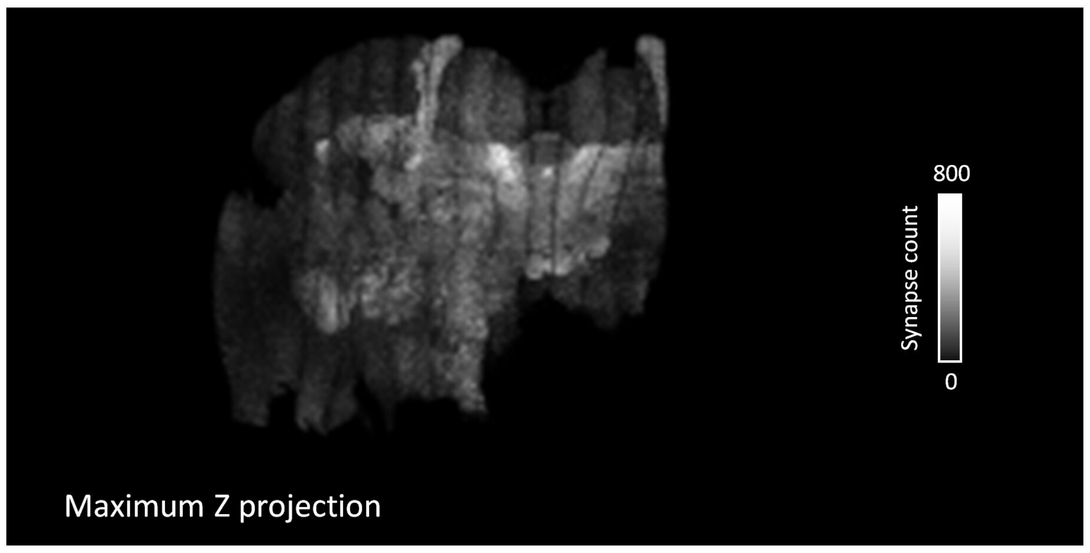

FlyEM synapse point cloud on resized FDA template

a

Input (post-synapses)

Output (pre-synapses)

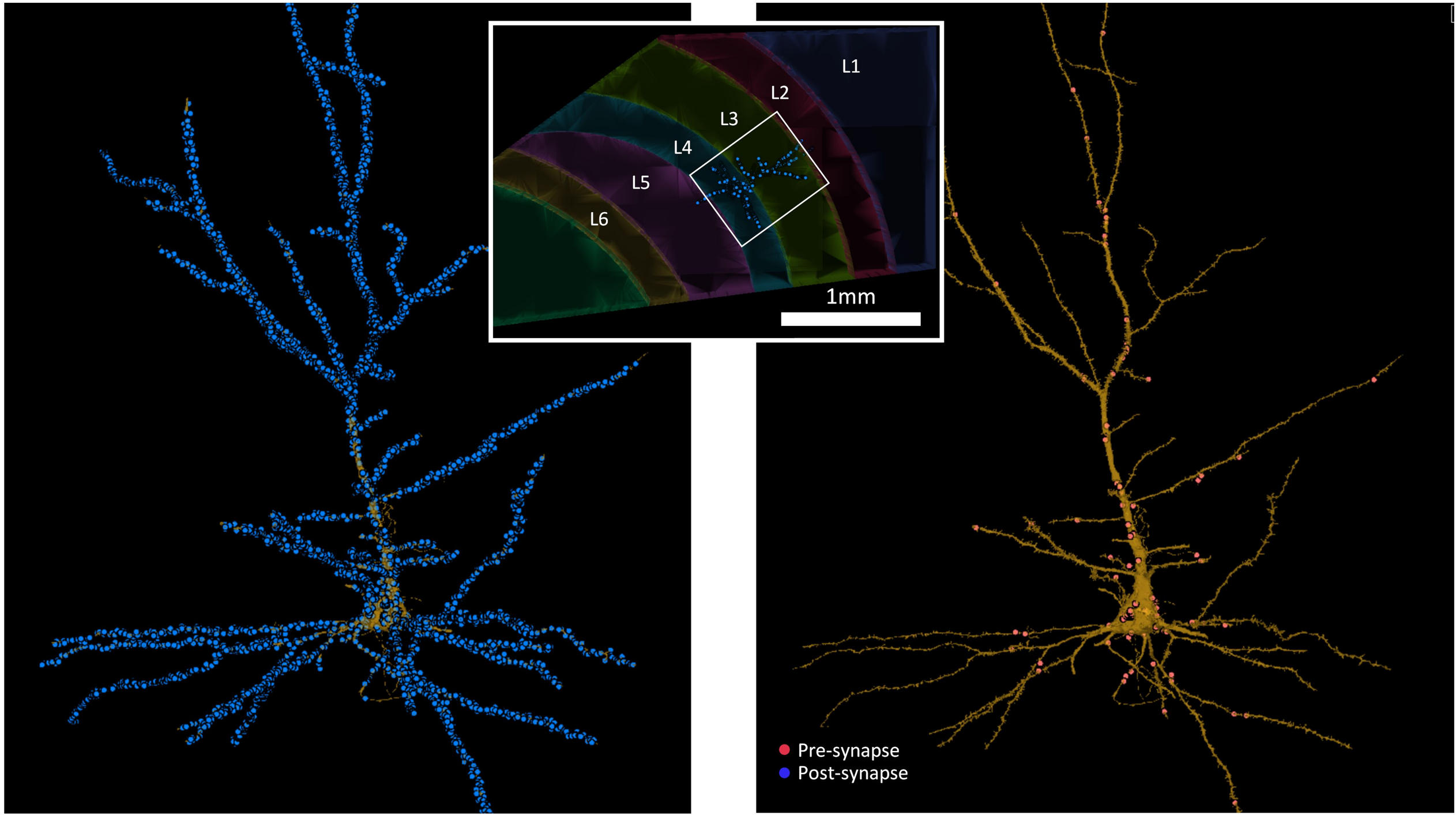

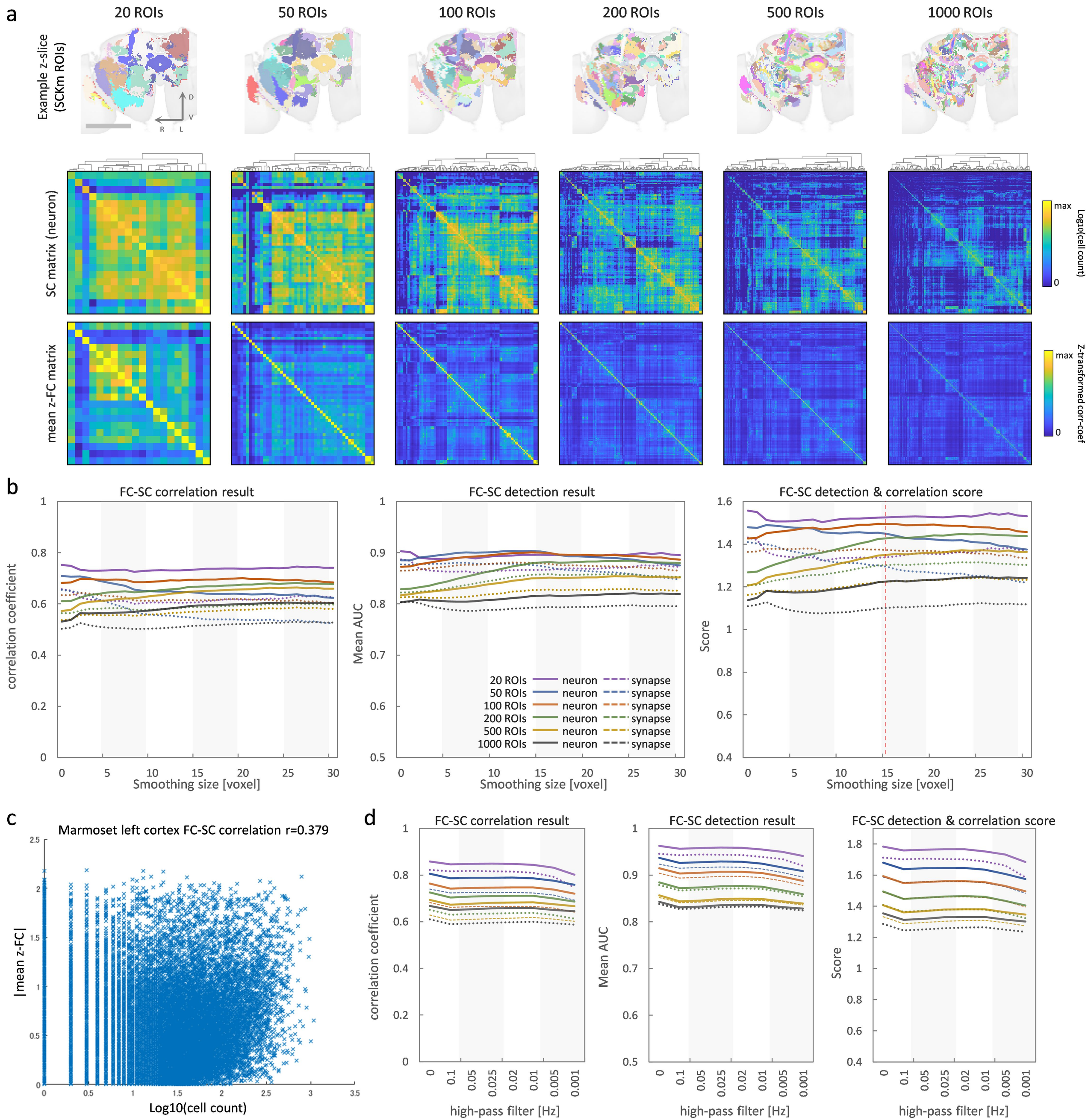
a
20 ROIs
50 ROIs
100 ROIs
200 ROIs
500 ROIs
1000 ROIs
Example z-slice (SCKm ROIs)
D
V
R
L
SC matrix (neuron)
mean z-FC matrix
max
0
Log10(cell count)
Z-transformed corr-coef
b
FC-SC correlation result
FC-SC detection result
FC-SC detection & correlation score
correlation coefficient
Mean AUC
Score
Smoothing size [voxel]
20 ROIs neuron synapse
50 ROIs neuron synapse
100 ROIs neuron synapse
200 ROIs neuron synapse
500 ROIs neuron synapse
1000 ROIs neuron synapse
c
Marmoset left cortex FC-SC correlation r=0.379
|mean z-FC|
Log10(cell count)
d
FC-SC correlation result
FC-SC detection result
FC-SC detection & correlation score
correlation coefficient
Mean AUC
Score
high-pass filter [Hz]

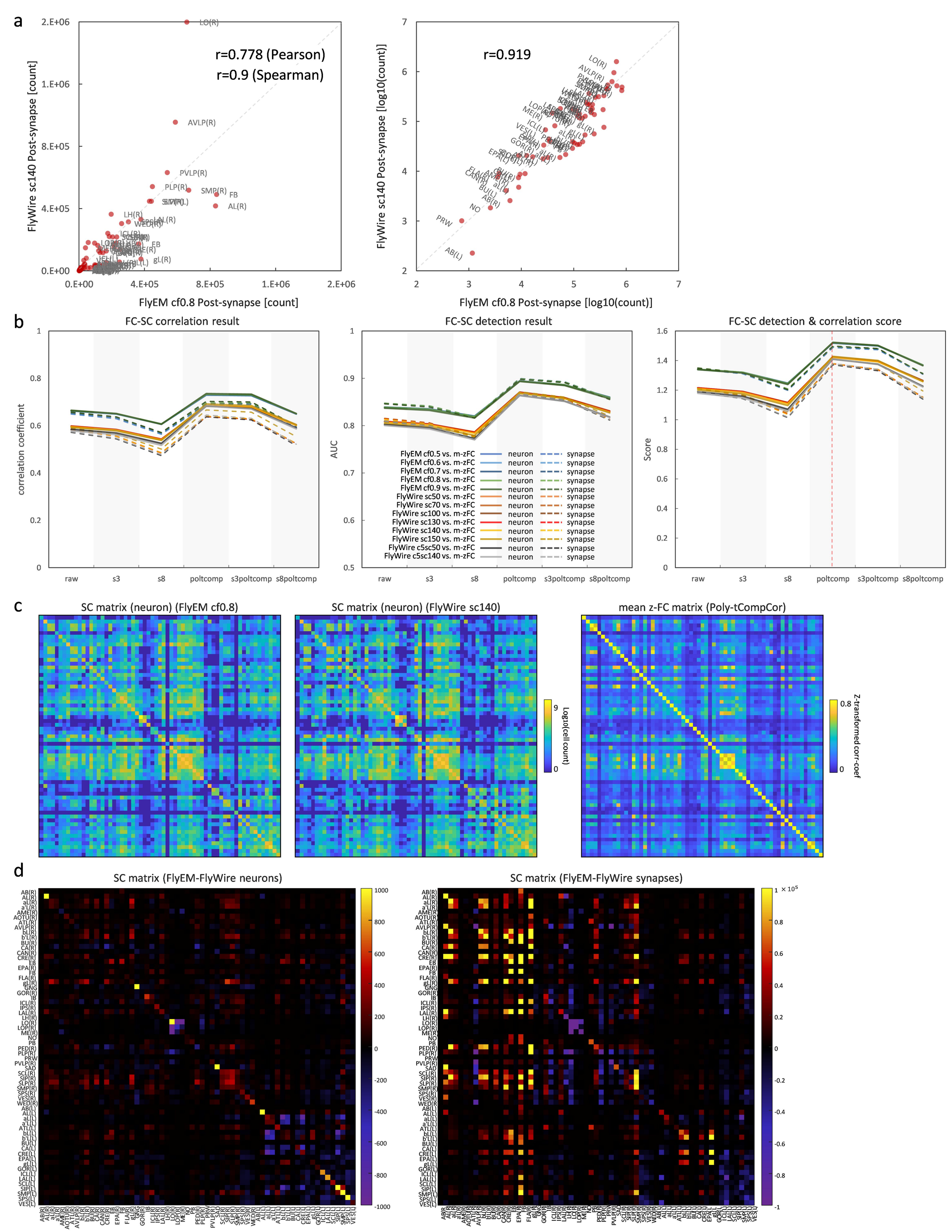
a
r=0.778 (Pearson)
r=0.9 (Spearman)
FlyWire sc140 Post-synapse [count]
FlyEM cf0.8 Post-synapse [count]
r=0.919
FlyWire sc140 Post-synapse [log10(count)]
FlyEM cf0.8 Post-synapse [log10(count)]
b
FC-SC correlation result
correlation coefficient
FC-SC detection result
AUC
FC-SC detection & correlation score
Score
raw
s3
s8
poltcomp
s3poltcomp
s8poltcomp
FlyEM cf0.5 vs. m-zFC
FlyEM cf0.6 vs. m-zFC
FlyEM cf0.7 vs. m-zFC
FlyEM cf0.8 vs. m-zFC
FlyEM cf0.9 vs. m-zFC
FlyWire sc50 vs. m-zFC
FlyWire sc70 vs. m-zFC
FlyWire sc100 vs. m-zFC
FlyWire sc130 vs. m-zFC
FlyWire sc140 vs. m-zFC
FlyWire sc150 vs. m-zFC
FlyWire c5sc50 vs. m-zFC
FlyWire c5sc140 vs. m-zFC
neuron
synapse
c
SC matrix (neuron) (FlyEM cf0.8)
SC matrix (neuron) (FlyWire sc140)
mean z-FC matrix (Poly-tCompCor)
Log10(cell count)
Z-transformed corr-coef
d
SC matrix (FlyEM-FlyWire neurons)
SC matrix (FlyEM-FlyWire synapses)

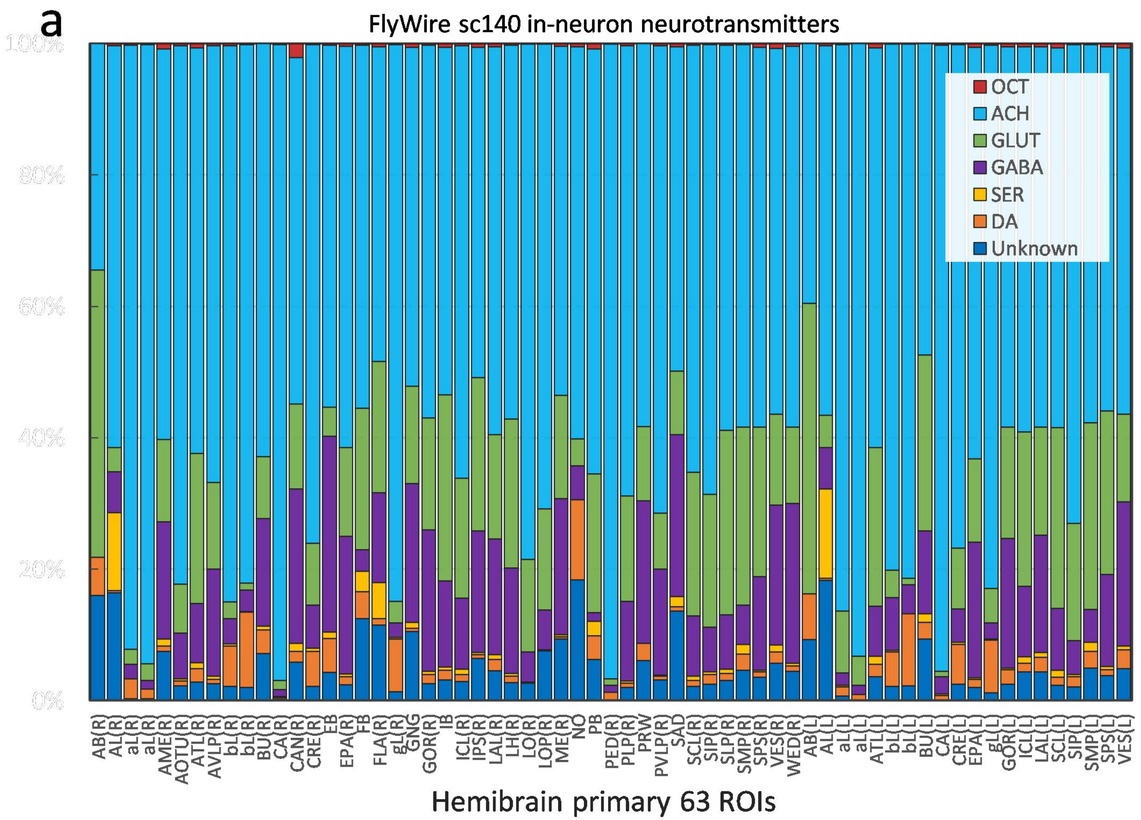
a
FlyWire sc140 in-neuron neurotransmitters
100%
80%
60%
40%
20%
0%
OCT
ACH
GLUT
GABA
SER
DA
Unknown
AB(R) AL(R) aL(R) aL(R) AME(R) AOTU(R) ATL(R) AVLP(R) bL(R) bL(R) BU(R) CA(R) CAN(R) CRE(R) EB EPA(R) FB FB FLA(R) gL(R) GNG GOR(R) IB ICL(R) IPS(R) LAL(R) LH(R) LO(R) LOP(R) ME(R) NO PB PED(R) PLP(R) PRW PVLP(R) SAD SCL(R) SIP(R) SLP(R) SMP(R) SPS(R) VES(R) WED(R) AB(L) AL(L) aL(L) aL(L) ATL(L) bL(L) bL(L) BU(L) CA(L) CRE(L) EPA(L) gL(L) GOR(L) ICL(L) LAL(L) SCL(L) SIP(L) SMP(L) SPS(L) VES(L)
Hemibrain primary 63 ROIs

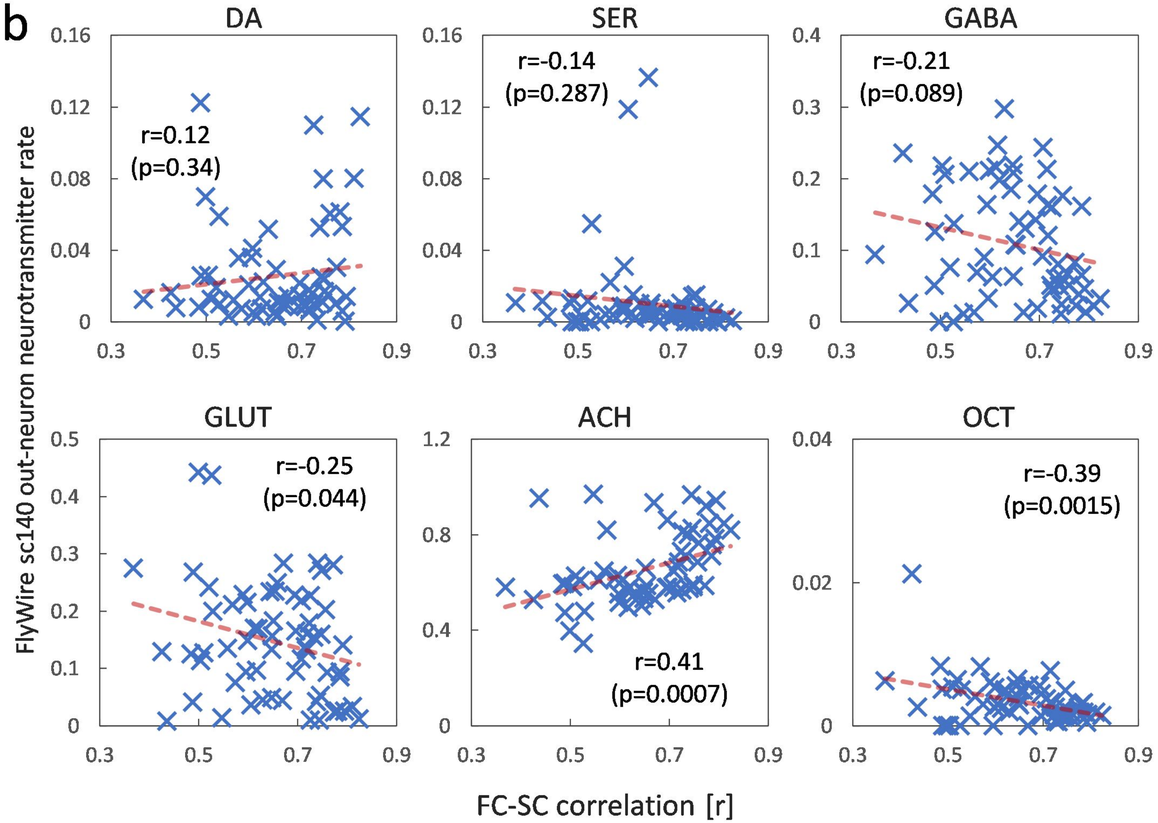
b
DA
r=0.12
(p=0.34)
SER
r=-0.14
(p=0.287)
GABA
r=-0.21
(p=0.089)
GLUT
r=-0.25
(p=0.044)
ACH
r=0.41
(p=0.0007)
OCT
r=-0.39
(p=0.0015)
FlyWire sc140 out-neuron neurotransmitter rate
FC-SC correlation [r]

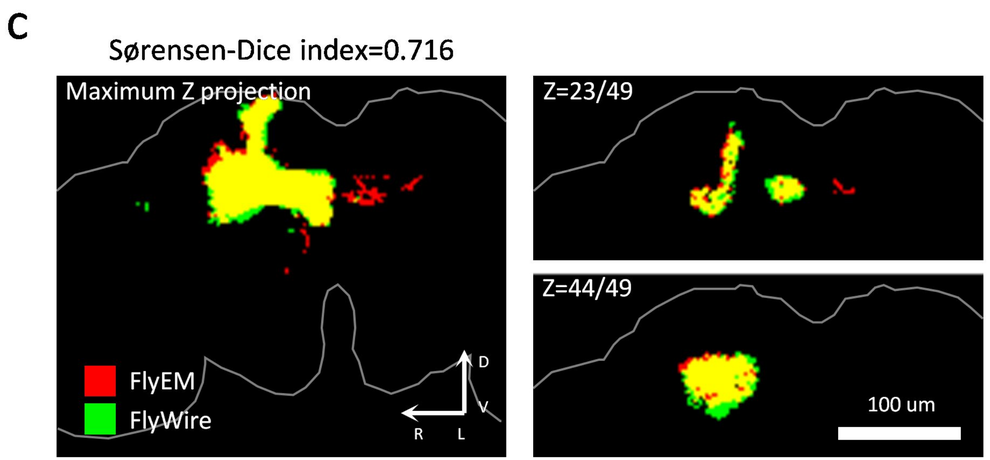
c
Sørensen-Dice index=0.716
Maximum Z projection
Z=23/49
Z=44/49
FlyEM
FlyWire
D
V
R
L
100 um

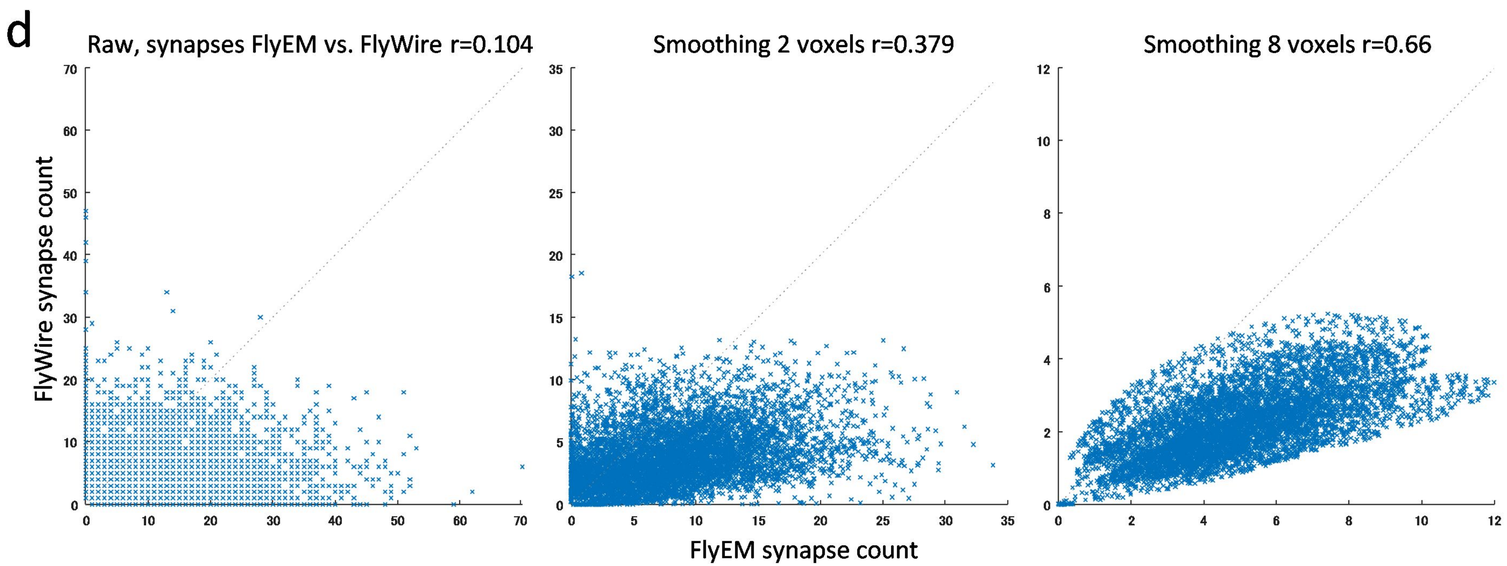
d
Raw, synapses FlyEM vs. FlyWire r=0.104
Smoothing 2 voxels r=0.379
Smoothing 8 voxels r=0.66
FlyWire synapse count
FlyEM synapse count

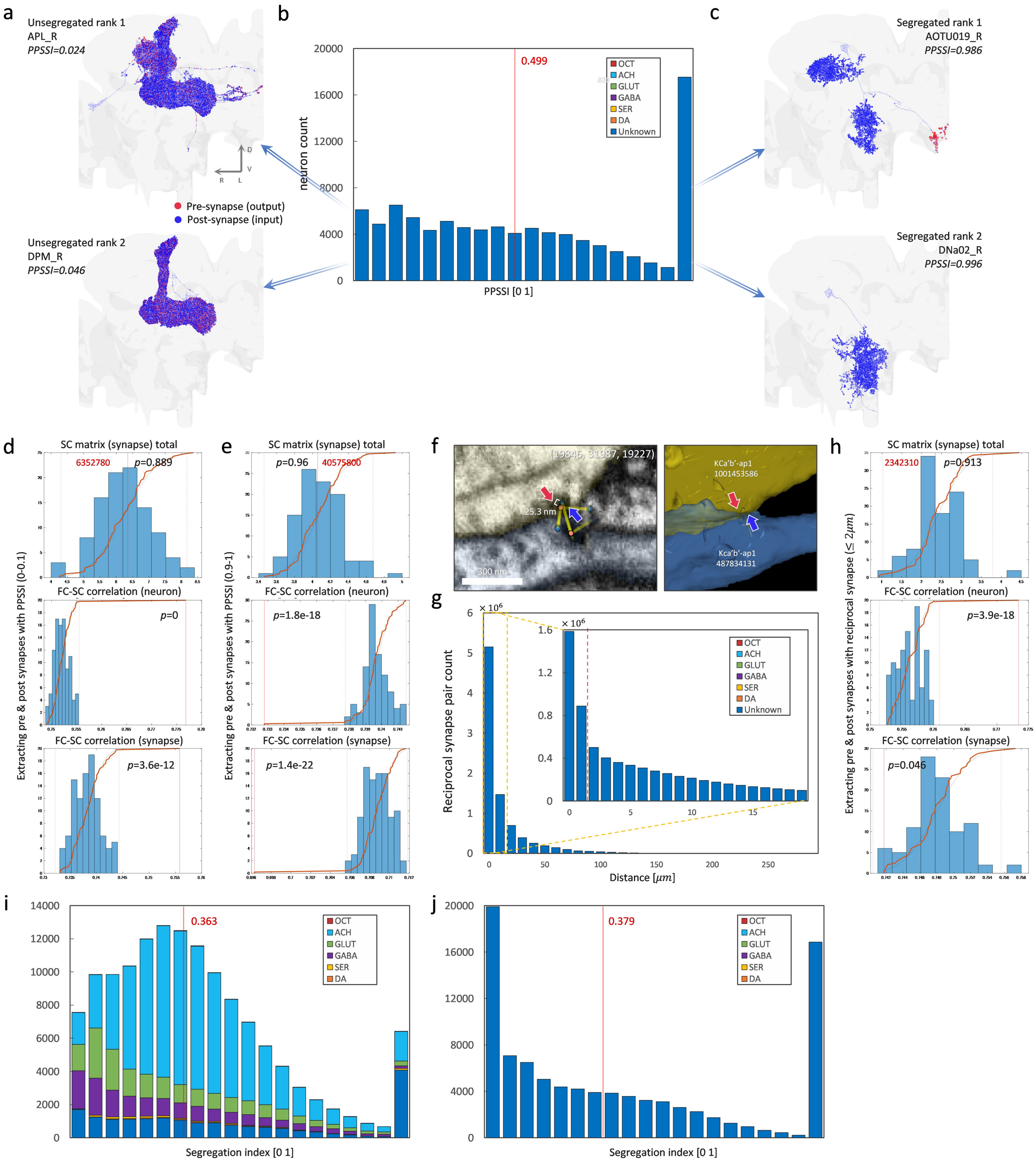
a
Unsegregated rank 1
APL_R
PPSSI=0.024
D
V
R
L
Pre-synapse (output)
Post-synapse (input)
Unsegregated rank 2
DPM_R
PPSSI=0.046
b
0.499
OCT
ACH
GLUT
GABA
SER
DA
Unknown
neuron count
PPSSI [0 1]
c
Segregated rank 1
AOTU019_R
PPSSI=0.986
Segregated rank 2
DNa02_R
PPSSI=0.996
d
SC matrix (synapse) total
6352780
p=0.889
FC-SC correlation (neuron)
p=0
FC-SC correlation (synapse)
p=3.6e-12
Extracting pre & post synapses with PPSSI (0-0.1)
e
SC matrix (synapse) total
p=0.96
40575800
FC-SC correlation (neuron)
p=1.8e-18
FC-SC correlation (synapse)
p=1.4e-22
Extracting pre & post synapses with PPSSI (0.9-1)
f
(19846, 31987, 19227)
25.3 nm
300 nm
KCa'b'-ap1
1001453586
Kca'b'-ap1
487834131
g
× 10^6
Reciprocal synapse pair count
Distance [μm]
OCT
ACH
GLUT
GABA
SER
DA
Unknown
h
SC matrix (synapse) total
2342310
p=0.913
FC-SC correlation (neuron)
p=3.9e-18
FC-SC correlation (synapse)
p=0.046
Extracting pre & post synapses with reciprocal synapse (≤ 2μm)
i
0.363
OCT
ACH
GLUT
GABA
SER
DA
Segregation index [0 1]
j
0.379
OCT
ACH
GLUT
GABA
SER
DA
Segregation index [0 1]

a

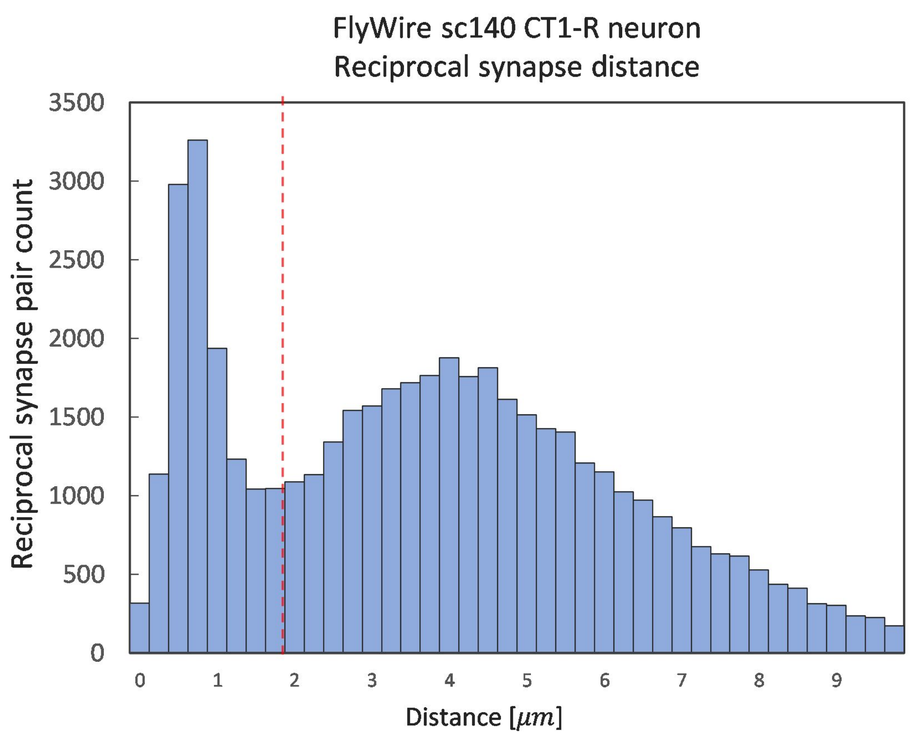

b

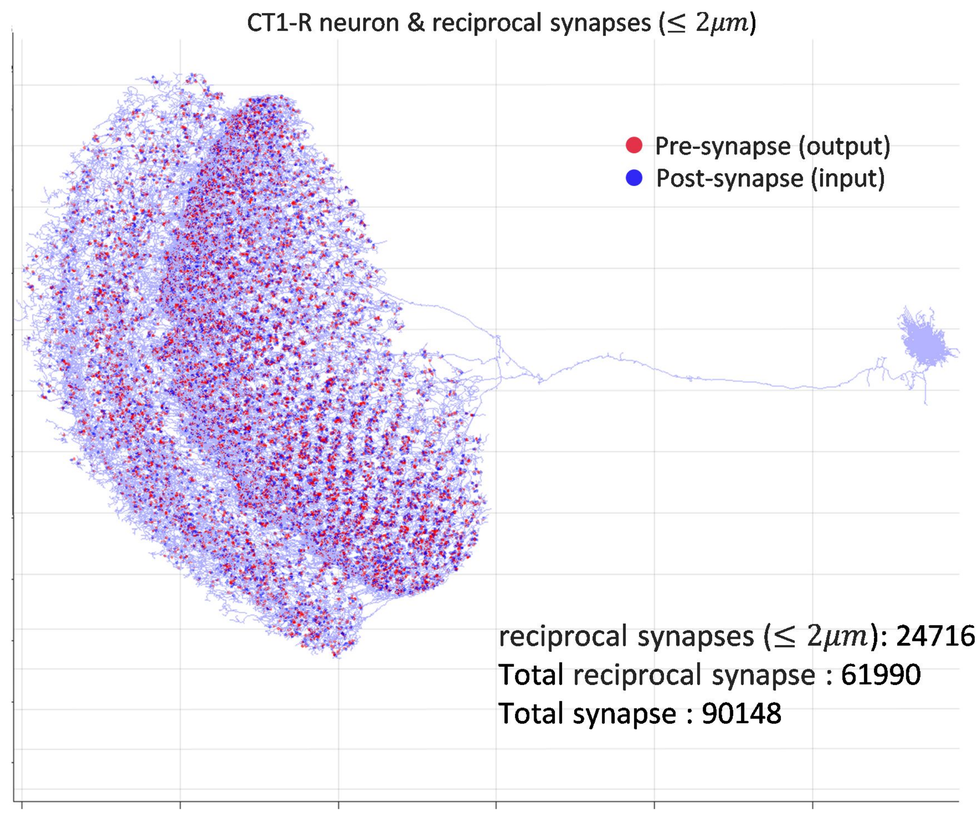

c

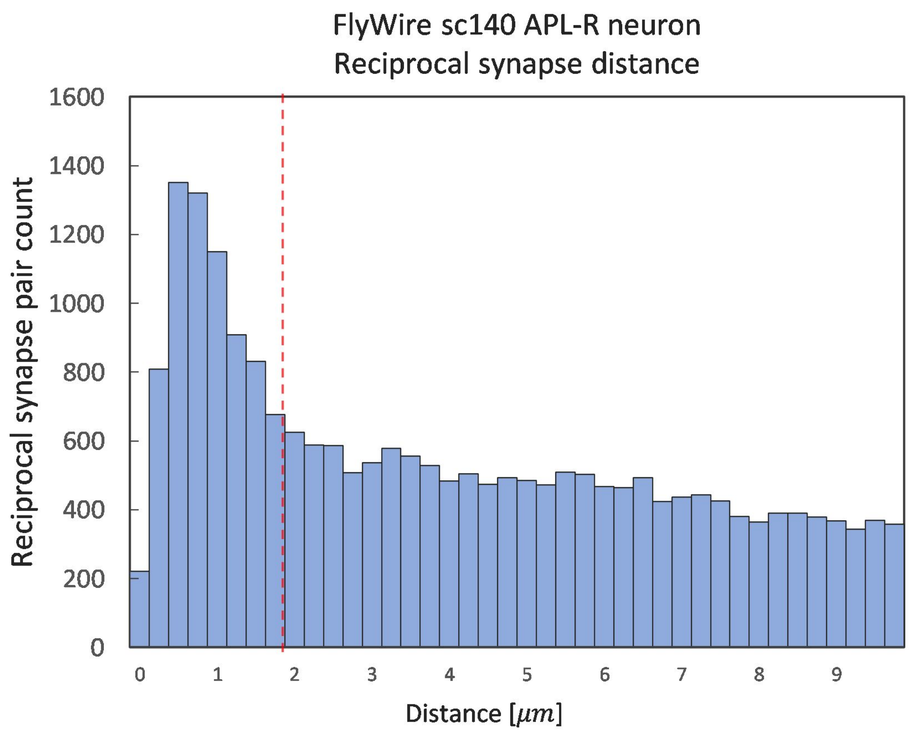

d

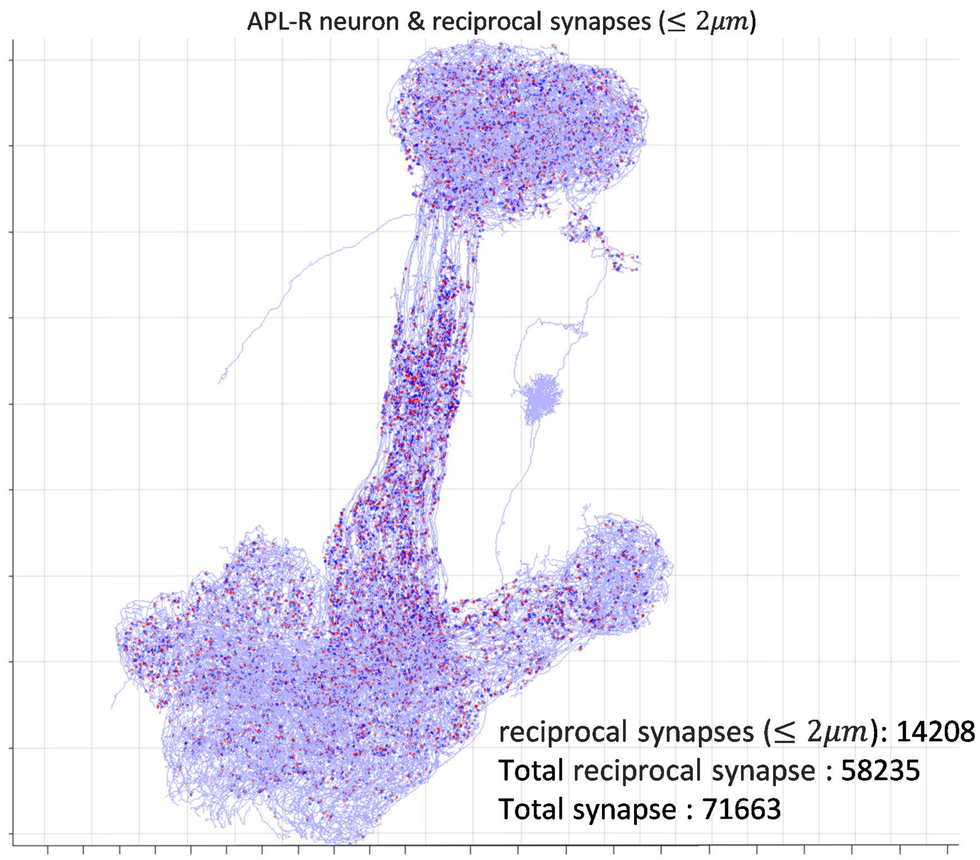

e Pre & post synapse point cloud within PPSSI (0-0.1)

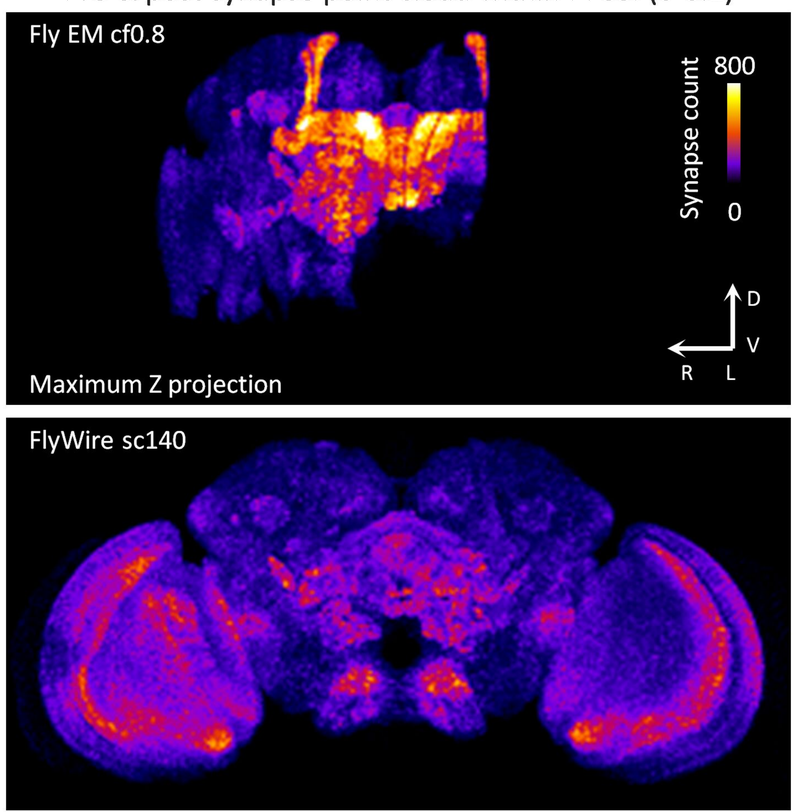

f Pre & post synapse point cloud within PPSSI (0.9-1)

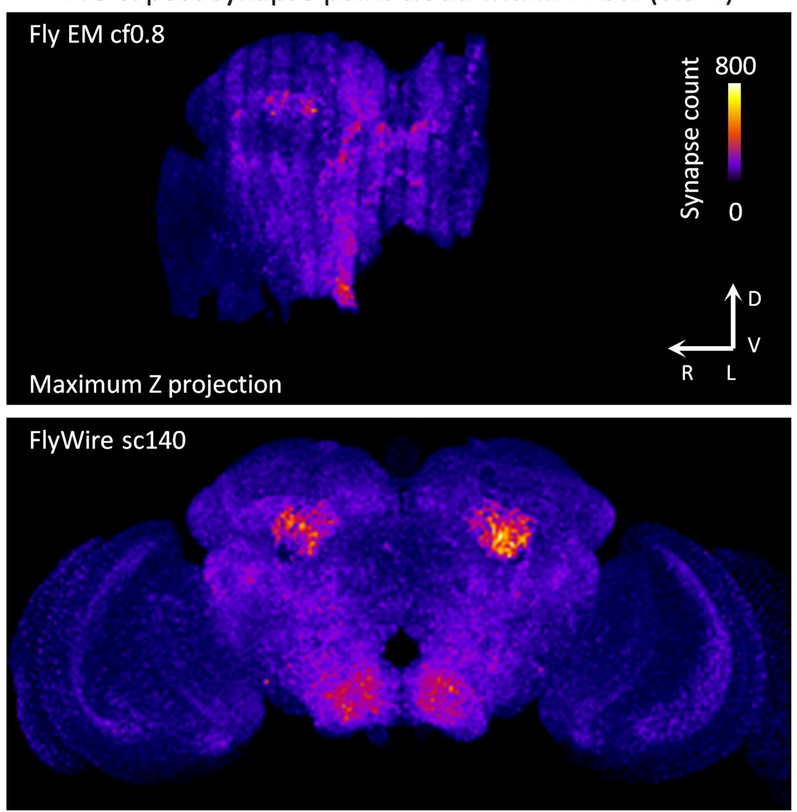

g Pre & post synapse point cloud of reciprocal synapse ($\leq 2\mu m$)

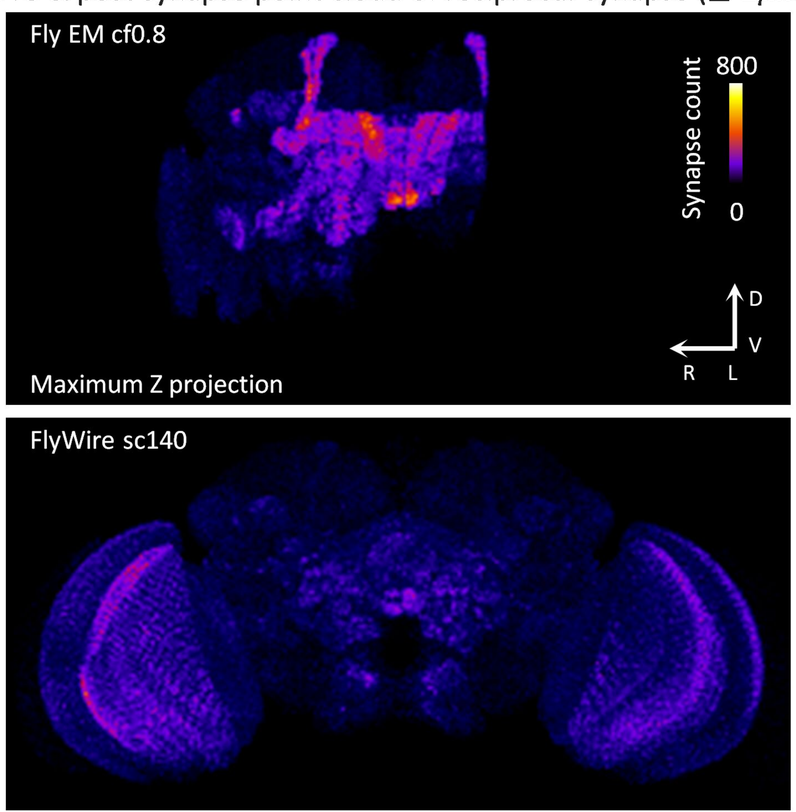

a
Unsegregated rank 3
APL_R (GABA)
PPSSI=0.022
Unsegregated rank 4
APL_L (GABA)
PPSSI=0.045
Unsegregated rank 5
Li33_R (GABA)
PPSSI=0.017
D
V
L
R
Pre-synapse (output)
Post-synapse (input)
Unsegregated rank 6
Li33_L (GABA)
PPSSI=0.020
Unsegregated rank 7
LPi15_R (GABA)
PPSSI=0.036
Unsegregated rank 8
LPi13_R (GABA)
PPSSI=0.040
Unsegregated rank 9
Li32_R (GABA)
PPSSI=0.022
Unsegregated rank 10
Sm42_R (GABA)
PPSSI=0.028
Unsegregated rank 11
LPi15_L (GABA)
PPSSI=0.040
b
Segregated rank 3
OA-AL2b2 (ACH)
PPSSI=0.973
Segregated rank 4
OA-AL2b2 (ACH)
PPSSI=0.966
Segregated rank 5
cL21_R (GABA)
PPSSI=0.935
Segregated rank 6
cL21_L (GABA)
PPSSI=0.939
Segregated rank 7
cM05_R (ACH)
PPSSI=0.924
Segregated rank 8
cL21_R (GABA)
PPSSI=0.934
Segregated rank 9
AN_multi_28 (GABA)
PPSSI=0.959
Segregated rank 10
cL21_L (GABA)
PPSSI=0.935
Segregated rank 11
AN_multi_28 (GABA)
PPSSI=0.964

a

Unsegregated rank 3
lLN2F_b(Full)_R
PPSSI=0.020

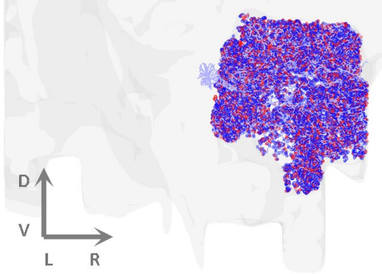

Pre-synapse (output)
Post-synapse (input)

Unsegregated rank 4
DPM_L
PPSSI=0.021

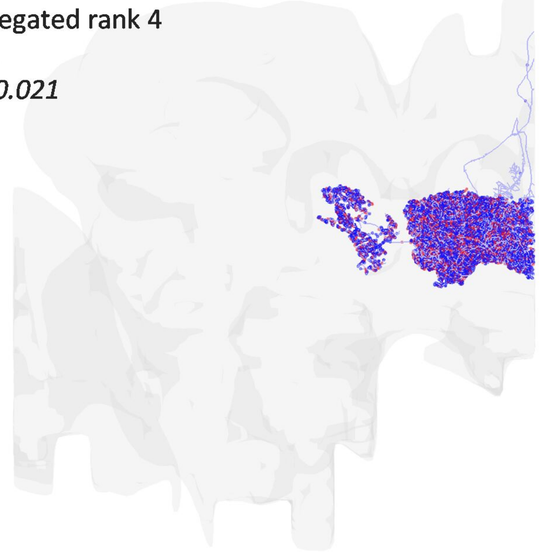

Unsegregated rank 5
PVLP011_R
PPSSI=0.020

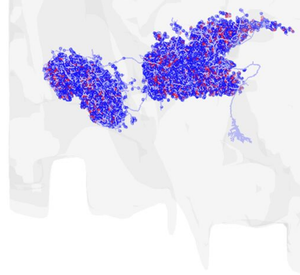

Unsegregated rank 6
lLN2F_b(Full)_R
PPSSI=0.027

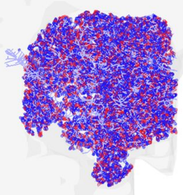

Unsegregated rank 7
lLN2F_a(Full)_R
PPSSI=0.010

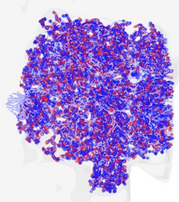

Unsegregated
rank 8
lLN2F_a(Full)_R
PPSSI=0.016

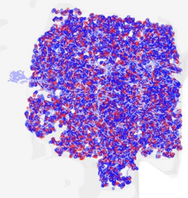

Unsegregated rank 9
lLN2T_b(Tortuous)_R
PPSSI=0.030

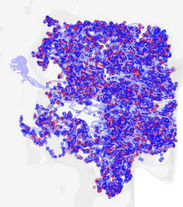

Unsegregated rank 10
v2LN30_R
PPSSI=0.015

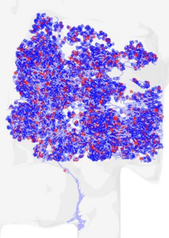

Unsegregated rank 11
lLN2T_b(Tortuous)_R
PPSSI=0.039

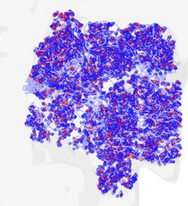

b

Segregated rank 3
MBON02(B2B'2a)_R
PPSSI=0.948

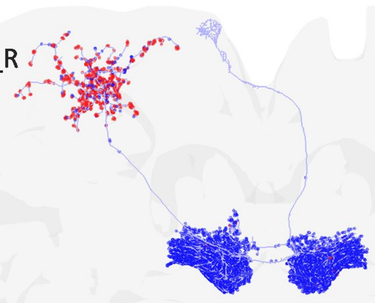

Segregated rank 4
MBON01(y5B'2a)_R
PPSSI=0.885

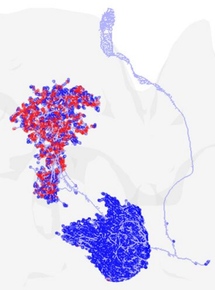

Segregated rank 5
MBON02(B2B'2a)_L
PPSSI=0.953

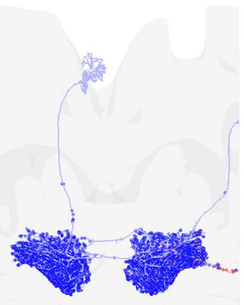

Segregated rank 6
DNa04_R
PPSSI=0.993

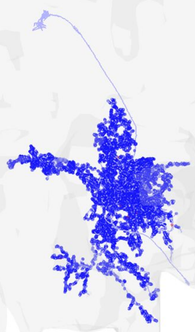

Segregated rank 7
Giant Fiber_R
PPSSI=0.962

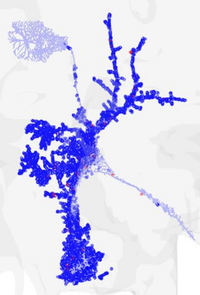

Segregated rank 8
MBON07(a1)_R
PPSSI=0.962

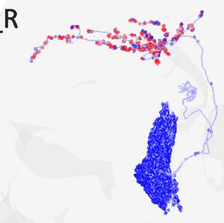

Segregated rank 9
MBON07(a1)_R
PPSSI=0.952

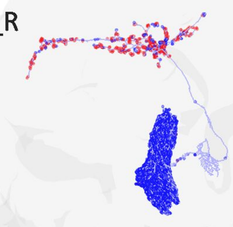

Segregated rank 10
PS017_R
PPSSI=0.998

Segregated rank 11
PVLP136_R
PPSSI=0.986

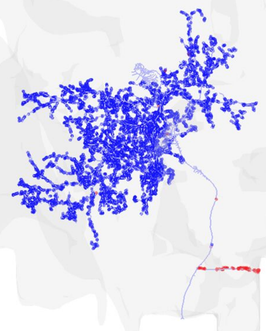

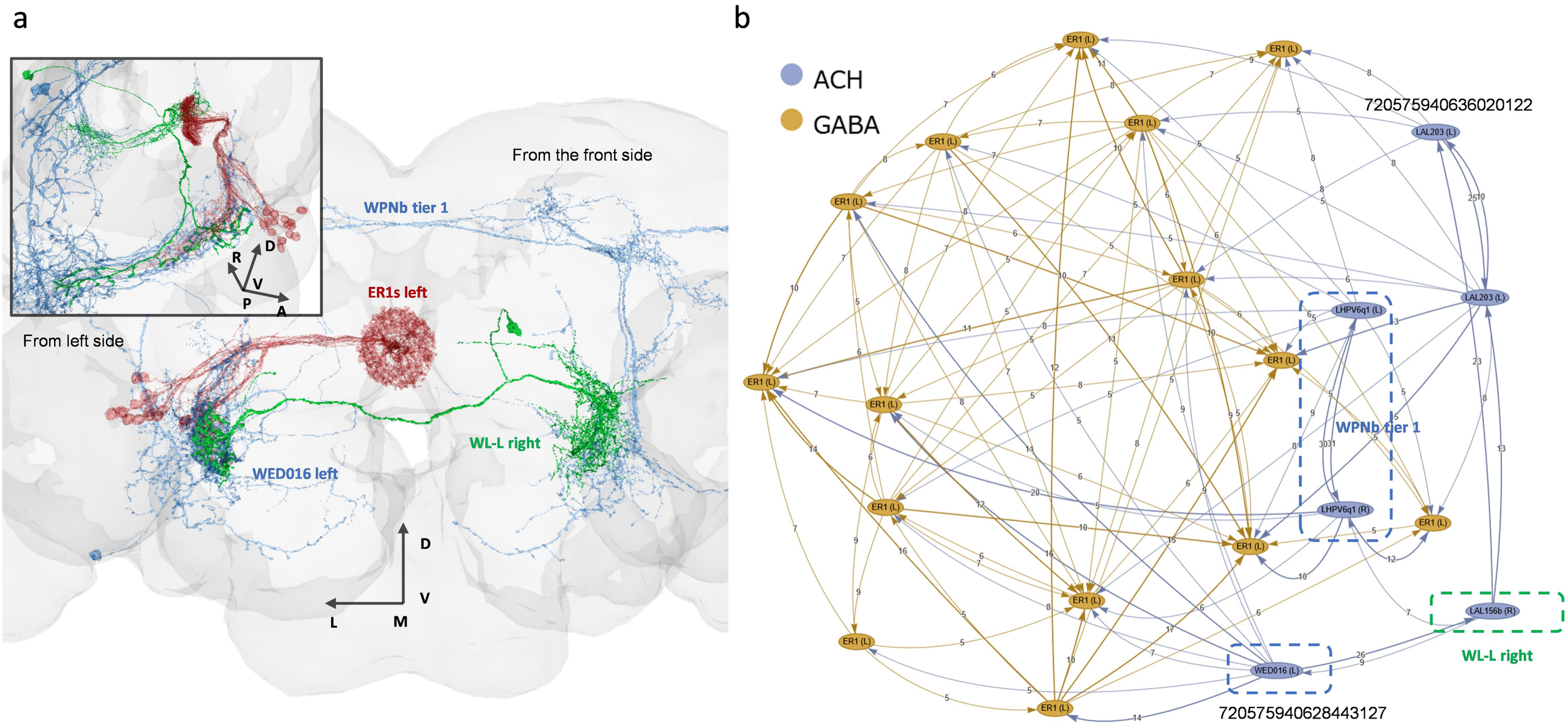
a
From the front side
WPNb tier 1
ER1s left
From left side
WL-L right
WED016 left
R
D
V
P
A
D
V
L
M
b
ACH
GABA
720575940636020122
LAL203 (L)
LHPV6q1 (L)
LHPV6q1 (R)
WPNb tier 1
LAL156b (R)
WL-L right
WED016 (L)
720575940628443127
ER1 (L)